Journal of Power Sources 274 (2015) 869–884

Contents lists available at ScienceDirect

Journal of Power Sources

journal homepage: www.elsevier.com/locate/jpowsour

Review

Significant impact of 2D graphene nanosheets on large volume change tin-based anodes in lithium-ion batteries: A review

Yang Zhao [a], Xifei Li [a, *], Bo Yan [a], Dejun Li [a, *], Stephen Lawes [b], Xueliang Sun [b, a, **]

[a] Energy & Materials Engineering Centre, College of Physics and Materials Science, Tianjin Normal University, Tianjin 300387, China
[b] Nanomaterials and Energy Lab, Department of Mechanical and Materials Engineering, University of Western Ontario, London, Ontario N6A 5B9, Canada

HIGHLIGHTS

- The significant impact of 2D graphene nanosheets on Tin-based anodes has been reviewed.
- Various Sn/graphene based binary, ternary composites have been summarized.
- The preparation methods, properties and mechanism of Sn/graphene composites have been concluded.
- The challenges and perspectives of this field have been reviewed as well.

GRAPHICAL ABSTRACT

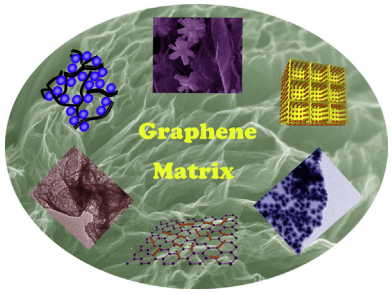

ARTICLE INFO

Article history:
Received 12 August 2014
Received in revised form
24 September 2014
Accepted 2 October 2014
Available online 4 November 2014

Keywords:
2D graphene
Tin-based anodes
Tin oxide
Stannate
Lithium-ion batteries

ABSTRACT

Sn-based materials have attracted much attention as anodes in lithium ion batteries (LIBs) due to their low cost, high theoretical capacities, and high energy density. However, their practical applications are limited by the poor cyclability originating from the huge volume changes. Graphene nanosheets (GNSs), a novel two-dimensional carbon sheet with one atom thickness and one of the thinnest materials, significantly address the challenges of Sn-based anodes as excellent buffering materials, showing great research interests in LIBs. In this review, various nanocomposites of GNSs/Sn-based anodes are summarized in detail, including binary and ternary composites. The significant impact of 2D GNSs on the volume change of Sn-based anodes during cycling is discussed, along with with their preparation methods, properties and enhanced LIB performance.

1. Introduction

As one of the most important energy-storage devices, lithium-ion batteries (LIBs) have attracted a lot of attention in both academic research and commercial applications, such as cell phones, laptops and digital cameras [1–5]. Despite many advantages over other competing electrochemical power sources, the use of LIBs exhibit some limitations when used in electric vehicles, hybrid electric vehicles and plug-in hybrid electric vehicles, since they require high energy density, good cycling performance and high rate capability [6–8]. As a result, the search for new anode and cathode materials providing enhanced electrochemical properties while remaining economical is always an ongoing study [9]. Graphite, as the commercialized anode material, has its own advantages, such as low and flat working potential, long cycle life and low cost [10]. On the other hand, graphite limits the lithium storage

* Corresponding authors.
** Corresponding author. Nanomaterials and Energy Lab, Department of Mechanical and Materials Engineering, University of Western Ontario, London, Ontario N6A 5B9, Canada.
E-mail addresses: xfli2011@hotmail.com (X. Li), dejunli@mail.tjnu.edu.cn (D. Li), xsun@eng.uwo.ca (X. Sun).

http://dx.doi.org/10.1016/j.jpowsour.2014.10.008
0378-7753/

performance in terms of energy and power densities due to the low theoretical capacity (LiC_6, 372 mAh g^{-1}) and low Li-ion transport rate (10^{-12}–10^{-14} cm^2 s^{-1}), respectively [11,12].

Of the alternative anode materials for LIBs, silicon shows great promise with a theoretical capacity of 4200 mAh g^{-1}. However, tin exhibits higher electrical conductivity and is less brittle than silicon. In addition, the preparation process of silicon anodes can be quite complex with poor controllability, inevitably increasing cost. Tin anodes shows higher volumetric capacity of about 2000 mAh cm^{-3} and gravitational capacity of 990 mAh g^{-1} than the commercial graphite as well as other transition metal oxide anodes (such as NiO, Co_3O_4, and Fe_2O_3, etc). Derivatives such as Sn-based alloys, tin oxides, tin sulfides, and stannates, are also attractive anode materials for LIBs. A significant advantage of Sn-based anodes over the commercial graphite is that they avoid solvent intercalation, and improve safety performance of LIBs. Moreover, the Sn based anodes exhibit lower potential hysteresis than transition metal oxides. Therefore, Sn based anodes have attracted tremendous interest as promising anode materials for LIBs. [13–20]. However, the practical application of Sn-based anodes is hampered by its poor cyclability, resulting from large volume changes of 259%, which results in electrical disconnection from conductive agents (e.g. carbon black) and the current collectors during the charge/discharge process [21,22]. The high potential hysteresis in the charge/discharge curves is an important concern for LIB applications. For example, very high potential hysteresis more than 1.0 V of the transition metal oxides (like NiO, Co_3O_4, Fe_2O_3, etc) seriously prevents their commercialization as anodes in LIBs. The characteristic Li–Sn alloying/de-alloying reactions are shown as shoulders between 0.4 V and 0.8 V, which are characterized by an acceptable potential hysteresis, enabling the commercialization possibility of these types of anodes. The hysteresis is partly related to the electrical conductivity of the active materials. The active materials with higher electrical conductivity exhibit the improved potential hysteresis, which originates from decreased electrochemical polarization. For instance, the $LiFePO_4$ cathodes combined with conductive materials such as carbon showed lower hysteresis than pristine $LiFePO_4$ [23]. In the case of anode side, it was reported that the metal oxide/carbon nanocomposites can also effectively improve the hysteresis problem [24–26]. Several approaches have been proposed to address the challenges of the large volume change anodes. One effective method is to assemble the active particles into different nanostructures [27,28], such as nanowires [29,30], nanospheres [31,32] , nanotubes [33–35], nanocubes [36,37] and hollow nanostructures [15,38–41]. The second method involves doping with an inactive element to reduce the volume change [42,43]. The third method is to make nanocomposites with an inactive/active matrix and stable components [40,44–49]. In the nanocomposites, the stable matrices act as a mechanical buffering zone against the large volume change of the active materials [44,50]. Effective matrices provide the conducting backbone for the active materials, and the soft structures are beneficial to buffering the internal stress of electrodes suffering from large volume change. Therefore, Sn-based nanocomposites with matrices have been demonstrated to effectively improve anode battery performance.

1.1. Li-storage properties of graphene

Graphene is a single layer of sp^2 carbon atoms arranged hexagonally and has generated enormous excitement for various potential applications because of its fascinating properties [51–62], such as a high intrinsic carrier mobility (200 000 cm^2 V^{-1} s^{-1}), excellent thermal conductivity (5000 W m^{-1} K^{-1}), high optical transmittance (~97.7%), high theoretical specific surface area (2630 m^2 g^{-1}), and superior mechanical strength [59].

As one of the new carbon materials, the Li-storage properties of graphene have been widely studied by numerous researchers [63–68]. P.C. Lian et al. and A. Shanmugharaj's group synthesized graphene nanosheets (GNSs) from graphite powder through oxidation followed by rapid thermal expansion in nitrogen atmosphere [69,70]. The different electrochemical properties of GNSs, expanded graphite and graphite have been compared as well [71]. The research results show that the reversible capacities of GNSs are almost double those of expanded graphite electrode and three times those of graphite electrode. D.Y. Zhao's group [72] prepared novel mesoporous graphene nanosheets (MGNs) with an excellent reversible capacity of 1040 mAh g^{-1} at 100 mA g^{-1} in the second cycle, and 833 mAh g^{-1} after 60 cycles. The atomically flat graphene layers with mesopores provide high contact surface area for lithium ion adsorption and intercalation, while the open mesopores in the orthogonal direction on the nanosheets offer efficient transport pathways for ion diffusion toward the deep portions of the stacked graphene layers thus delivering excellent lithium ion storage capacity and cycling performance [72]. Several researchers reported that the greatly improved capacities in disordered GNSs are mainly ascribed to additional reversible storage sites such as edges and other defects [58,73–75]. However, it should be noted that high surface area of graphene increased the contact area between the anode and the electrolyte, which results in more SEI formation in the first discharge [76]. For example, GNSs could show a high discharge capacity of 1233 mAh g^{-1}, but its high surface area resulted in a low Coulombic efficiency of 54% with irreversible capacity of 672 mAh g^{-1}. In our previous studies [77], three types of GNSs with varying size, edge sites, defects and number of layers have been successfully created. It was demonstrated that controlled morphologies and microstructures of GNSs have important effects on the cyclic performance and rate capability of LIBs. Meanwhile, the specific functional groups can further enhance the reversible capacity of reduced graphene [78]. The capacity at potentials greater than 1.5 V is predominantly attributed to phenol groups, while the capacity of the redox couple at 1.1 V results from cyclic edge ether groups.

Nitrogen (N) or boron (B) as a dopant and/or N/B-containing functional groups was employed to enhance the GNSs performance [79–88]. For doped GNSs, the intense growth of the disorder-induced D band indicates that Li^+ intercalation/de-intercalation into graphene sheets upon cycling brings about a more noticeable change in the degree of long-range ordering in the hexagonal lattice than that of GNSs [88]. H.M. Cheng et al. [89] reported an electrode made with heteroatom (N, B)-doped chemically derived GNSs that exhibited extremely high rate performance and large capacity. The doped GNSs showed a high reversible capacity of >1040 mAh g^{-1}. In another study, X.L. Feng's group [89,90] developed a facile approach to synthesize free-standing fully fluorinated GNSs, which have high capacity, high rate capability and stable cycling performance. The effects of the electron-deficient N-doped GNSs on lithium storage were investigated via first-principles calculations [91], and the enhanced reversible capacity was attributed to the N-doped system. It was concluded that the unique 2D structure, disordered surface morphology, heteroatom defects, better electrode/electrolyte wettability, increased inter-sheet distance, and improved electrical conductivity of the doped graphene are beneficial to Li-storage performances and thus show significant advantages for LIB anodes in comparison to those of pristine chemically derived graphene and other carbonaceous materials [89,92].

The complex and interesting folded structures of GNSs have attracted much attention, since the folding of a structure can change its form and functionality, which may induce new and

distinct properties in GNSs [93–95]. Thus, various flexible graphene papers (GPs) have been designed. Vacuum filtration is the mostly widely used approach for the development of GPs [96] and the flexible structure of GPs makes them potential anodes for free standing batteries. In our previous research, we studied in detail the influence of GP thickness on its electrochemical performance [97]. We concluded that the capacity decline with the increase of GP thicknesses is associated with the dense restacking of GNSs and a large aspect ratio of GPs. The effective Li^+ diffusion distance in GPs is mainly controlled by the thicknesses. The diffusion proceeds mainly in the in-plane direction, while cross-plane diffusion is restrained. As such, the effective contact of GNSs with electrolyte is limited and the efficiency of carbon utilization is very low in the thick GPs. However, the unique feature of graphene will be lost when the GNS are assembled into GPs, in which they are closely stacked. Thus, access of electrolyte to the GNS is restrained and consequently, a barrier for Li diffusion into the GNS is established, leading to lower specific capacities of GPs [97,98]. In addition, the multi-layer graphene/single-walled carbon nanotube flexible free-standing film electrodes were prepared by a time-efficient microwave autoclave method [99]. The flexible film exhibited good charge capacity of about 303 mAh g^{-1} after 50 cycles. The presence of carbon nanotubes in the electrodes, which forms a unique sandwich structure with GNSs, can provide efficient conductive pathways to improve the ionic conductivity, further enhancing the electrochemical properties of GPs. Thus, for the development of flexible GP-based anodes, pure GPs will not be adopted;the trend has been for researchers to develop complex films with Sn or Si nanomaterials to enhance the properties of GPs.

1.2. The advantages of graphene for Sn-based anodes

GNSs have great research interests as buffering materials for large volume change Sn-based anodes in LIBs, owing to their remarkable features: (i) the high flexibility of graphene could be an excellent supporting matrix or coating layer. During the charge/discharge processes, the volume expansion and particle aggregation would be relieved by the buffering GNSs. (ii) The rich functional groups at the GNS surface can serve as an appealing 2D substrate for the anisotropic growth of various Sn-based materials [100]. (iii) The high intrinsic surface area and outstanding electrical conductivity of GNSs provide an ideal platform for the storage and transportation of lithium ions and electrons [100]. As a result, a lot of effort has been devoted to introducing GNSs into Sn-based anode materials, and a large number of papers have been published based on this idea [101–108]. Sn-based anode materials for LIBs have many merits, such as low cost, high theoretical capacities, and high energy density. However, volume expansion/contraction limits further improvements to the anode performance. The flexibility and high conductivity of graphene makes it an excellent matrix material. The introduction of graphene into Sn-based anode materials addresses the problems of large volume changes, resulting in high reversible capacity, rate capability and structural stability of the composites. The importance strongly motivates us to review the significant effects of graphene as excellent matrix on large volume change Sn-based materials as potential anodes for LIBs. It is important to review the recent achievements and development of GNSs as an excellent matrix to address the challenges of large volume change Sn-based anodes in LIBs. To date, few review papers have focused on this topic in detail. In this review article, we mainly focus on how a matrix of 2D GNSs mitigates the problems of Sn-based anodes originating from large volume change upon cycling, including their preparation methods, properties and enhanced LIB performance. The important effects of GNS doping are also reviewed.

2. Sn/graphene-based binary composites

2.1. Sn/GNS composites

Based on the advantages of GNSs, Sn/GNS composites have been widely studied with continuous exploration of GNSs [101,109,110]. Via microwave reduction [111], Sn/GNSs composites were synthesized with a stable reversible capacity of about 500 mAh g^{-1}. Other improvements have been reported with Sn-nanoparticle/GNS nanocomposites [112]. As shown in Fig. 1(e), the optimized Sn/GNS electrode exhibits improved reversible capacity and cycling stability (838.4 mAh g^{-1} after 100 cycles).

It has been found that the morphologies and particle sizes of Sn composites with GNSs have a critical influence on the electrochemical performance of the nanocomposite. G.X. Wang et al. [113] studied the Sn/graphene nanocomposites synthesized by a combination of a microwave hydrothermal approach and a one-step hydrogen gas reduction. The prepared composite anodes with smaller Sn particle size (10–20 nm, see Fig. 1(b)) exhibit an initial discharging capacity of 946 mAh g^{-1} and a reversible charging capacity of 542 mAh g^{-1}, which is better than anodes made with larger particles (60–120 nm, see Fig. 1(a)). It is considered that the smaller particle sizes on the graphene will effectively reduce the pulverization and cracking of Sn nanoparticles. The reduced particle size can significantly increase the rate of lithium insertion/extraction, because of the short distances for lithium-ion transport within the particles. To some degree, the smaller particles of Sn can reduce the pulverization and cracking due to the decrease of absolute volume change, resulting in the enhancement of electrochemical performances [114,115]. However, the increased reversible capacity and cycling stability of the pure Sn nanoparticles are still not satisfied for the practical application because the proposed nanoscale strategy does not fully address the volume change problem of the anodes. In addition to using nanosized Sn, the existence of graphene in the composites can further relieve the volume expansion/contraction of Sn nanoparticles [27]. Another approach for Sn/GNS composites is to design an ingenious structure of Sn in order to relieve the volume expansion and the increasing lithium ion expansion coefficient. Using a conventional film deposition and annealing process, multilayer nanocomposites of Sn-nanopillar arrays sandwiched between graphene layers were obtained (Fig. 1(c)) and exhibit similar performance [10]. The composites show higher reversible capacity and excellent cycling performance at a current density of 5 A g^{-1}. The 1D Sn nanopillars and 2D graphene layers enable efficient transport of both Li ions and electrons while offering morphological flexibility to hamper structural failure during cycling. The enhanced electrochemical performance of both composites can be attributed to the highly conductive GNS matrix, the high specific surface area of tin nanoparticles and the synergy between the GNSs and Sn nanoparticles [10,113]. The existence of 2D layered GNSs highly inhibit the aggregation of Sn-based nanoparticles. Moreover, Sn-based nanoparticles between graphene layers efficiently suppress the restacking of graphene. Thus, the composites show a beneficial synergistic effect between graphene and Sn based nanoparticles.

As a matrix, the morphology and structure of graphene have a remarkable effect on the Li-storage properties of the nanocomposite. The Sn@GNS nanostructure was synthesized in situ into a vertically aligned graphene host that sandwiches the nanostructures [116] and exhibited larger-than-theoretical reversible capacities of 1037 mAh g^{-1} even after prolonged cycling, in addition to a coulombic efficiency of more than 97%. In another study, a novel structure of graphene networks anchored with Sn@GNS was synthesized using an in situ CVD technique using metal precursors as a catalyst and three-dimensional self-assembled NaCl particles

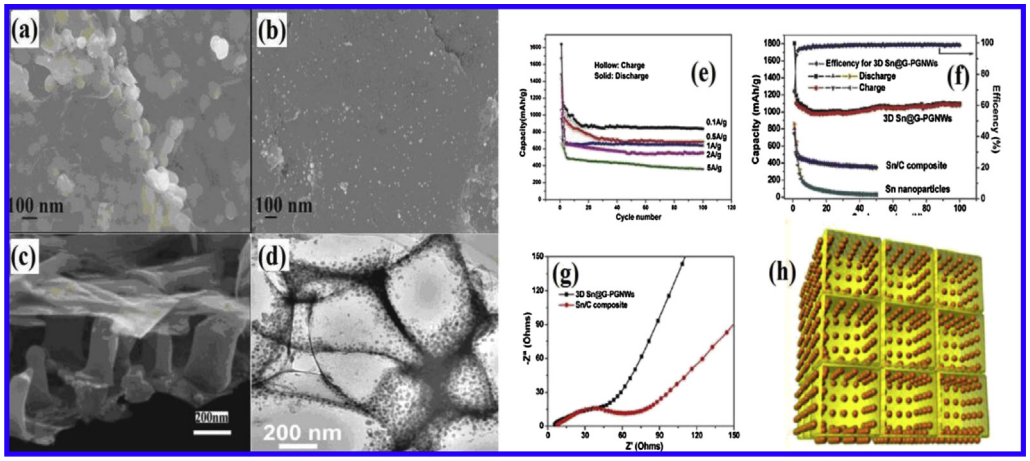

Fig. 1. SEM images of Sn/graphene nanocomposites with different particle sizes (a, b); Reproduced from Ref. [113]; SEM images of the Sn-nanopillar/graphene nanostructures (c); Reproduced from Ref. [10]; graphene networks anchored with Sn@Graphene composites (d); Reproduced from Ref. [117]; cycling performance of Sn/GNS electrode (e), and graphene networks anchored with Sn@Graphene composites (f); Reproduced from Refs. [112,117]; Nyquist plots of 3D Sn@G-PGNWs and Sn/C composite over the frequency range from 100 kHz to 0.01 Hz (g); Schematic illustration of 3D Sn@G-PGNWs (h); Reproduced from Ref. [117].

as a template [117] (seen in Fig. 1(h)). As shown in Fig. 1(d), a series of novel 3D porous graphene networks are anchored with small and uniform Sn nanoparticles encapsulated with graphene shells. As a result, long-term cyclic stability at high rates (a high capacity of 682 mAh g^{-1} is achieved at 2 A g^{-1} after 1000 cycles) and superior capacity (1022 mAh g^{-1} at 0.2 C) were achieved, as shown in Fig. 1(f). The uniquely designed structure of both composites, which provide ultra-thin, flexible graphene sheets to accommodate changes in volume, introduces large surface areas, high electrical conductivity, and shortened transportation lengths for both Li ions and electrons, contributing to its excellent performance [116]. Meanwhile, the graphene shells with high elasticity can effectively maintain the structural and interfacial stabilization of Sn nanoparticles as well as accommodate the mechanical stress resulting from the severe volume change of the anodes [117].

Furthermore, electrochemical impedance spectroscopy analysis was used to understand the much higher performance of the composites. The medium-to-high-frequency depressed semicircle and a low-frequency linear tail are consistent with impedance spectra of the previous Sn-based anodes. The semicircle at high frequency is an indication of SEI resistance (R_{SEI}) and contact resistance (R_f), the semicircle across the medium-frequency region represents the charge-transfer impedance (R_{ct}) on the electrode/electrolyte interface, and the low-frequency linear tail corresponds to the Warburg impedance (Z_w) associated with the diffusion of lithium ions in the bulk electrode (R_e). It can be found clearly that the diameter of the semicircle for the 3D Sn@G-PGNW electrode in the high–medium-frequency region is significantly smaller than that of the Sn/C composite, which illustrates the superior rate performance of the 3D Sn@G-PGNW hybrid anode as well as implies that the CVD-synthesized graphene and 3D porous graphene structure could effectively enhance the electrical conductivity and reduce the contact and charge-transfer resistances in the Sn@G-PGNW electrode. [117].

2.2. Tin oxide/graphene composite

Different from a Sn anode, SnO_2 initially reacts with lithium to form Sn and Li_2O. Then the produced Li_2O can serve as a "cushion" to buffer the large volume change during alloying and dealloying of Sn with lithium, which is an important reason why the cyclability of SnO_2 is better than that of Sn [118,119]. However, the performance of SnO_2 anodes still does not satisfy commercial requirements. The commercial requirements of anode materials can be summarized as i) large reversible capacity; ii) stable performance and long cycle life; iii) stability of the electrode and no side reactions with the electrode; and iv) low cost and environmentally friendly. Thus, recent research interest has involved improving their electrochemical performance by designing a variety of nanostructures, such as SnO_2 nanowires [120–122], SnO_2 nanotubes [34,35,123], SnO_2 nanosheets [124–127], 3D SnO_2 nanoflowers [128], and hollow nanostructures [41,129,130]. Similar to Sn anodes, combining SnO_2 with a buffering system like carbon [39,116,131–133], carbon nanotube [134–137], conductive polymer [138–140] or graphene, is an effective approach to improve performance. Importantly, it has been demonstrated that SnO_2/GNS composites significantly enhance battery performance [102,141–146].

The SnO_2/GNS composites have been fabricated in a number of reports using different methods [124,141–144,147–154]. A classical work of SnO_2/GNS has been done by I. Honma [141], in which the schematic illustration for it is shown in Fig. 2(g). Another simple wet chemical method was proposed to synthesize the SnO_2/graphene composites [155]. And a special structure of SnO_2 nanoparticles entrapped in a graphene framework [156] was synthesized by covalently linking SnO_2-anchored graphene oxide layers with diboronic acids. In our previous research [119], SnO_2-graphene nanosheets (SnO_2/GNS) containing both amorphous and crystalline SnO_2 phases were fabricated via advanced atomic layer deposition (ALD). The different morphologies of both composites can be seen in Fig. 2(e, f), in which the dimensions of the crystalline SnO_2 nanoparticles were in the range of 30–40 nm, while the amorphous ones were in the range of 3–5 nm. As a result, it was observed that the SnO_2/GNS nanocomposites achieve good cycling performance (a high capacity of 793 mA h g^{-1} in 150th cycle). The results demonstrated that amorphous SnO_2-GNS is more effective than the crystalline SnO_2-GNS in overcoming the electrochemical and mechanical degradation of SnO_2. The morphological evolution of the crystalline SnO_2-GNS and the amorphous SnO_2-GNS is suggested in Fig. 3 (e, f). The introduction of GNSs into the SnO_2-based nanocomposite improves performance by increasing its electrical conductivity and releasing strain energy [119,157]. Moreover, controlling the size of the SnO_2 nanoparticles in the SnO_2/GNS composites is critical for anode performance. For example, an anode consisting of small SnO_2 nanoparticles in an electronically conductive graphene network

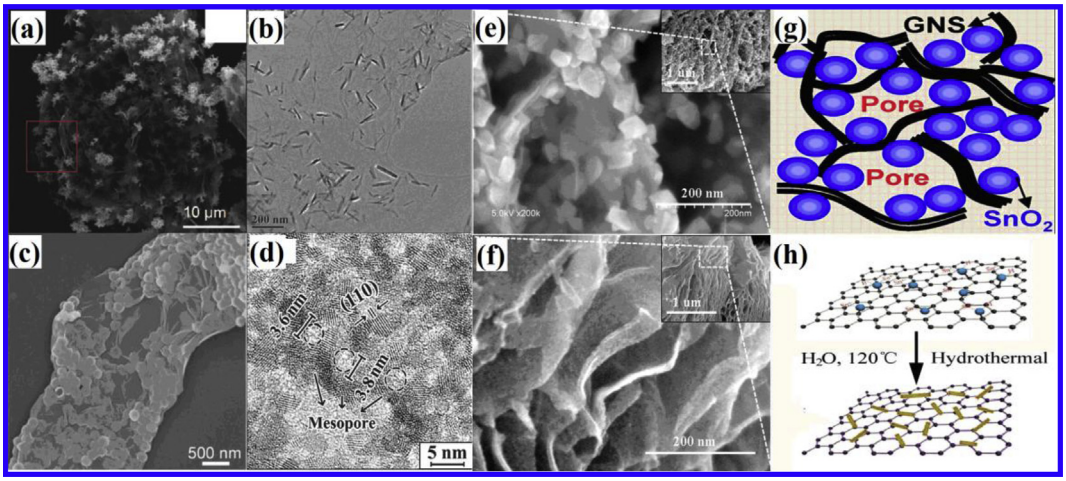

Fig. 2. SEM images of flower-like SnO_2/graphene composites (a); Reproduced from Ref. [160], and hollow sphere SnO_2/graphene composites (c); Reproduced from Ref. [161]; TEM images of nanorod SnO_2/graphene composites (b), and a mesostructured graphene-based SnO_2 composite (d); Reproduced from Refs. [146,162]; SEM observation of crystalline (e) and amorphous (f) SnO_2-GNS; Reproduced from Ref. [119]; Schematic Illustration for the SnO_2/graphene composites (g); Schematic diagram of the one-step hydrothermal synthesis of SnO_2/GS (h); Reproduced from Refs. [141,146].

delivers a superior cyclability, with capacities of 1813 mAh g^{-1} after over 1000 cycles under a high current density of 2 A g^{-1} [157]. The reasons for such high capacities are: (1) the ultra-small sizes of the SnO_2 particles partially initiated a reversible conversion between SnO_2 and Li_2O upon cycling, and accommodated the volume changes during the charge–discharge process. (2) The graphene network not only enhanced the conductivity of the composite but could also reversibly accommodate a large amount of lithium. (3) The severe expansion–contraction of SnO_2 during lithiation–delithiation resulted in the graphene being mesoporous with more activated sites for Li storage. (4) The polymeric gel-like film formation as a result of electrolyte decomposition contributed to extra capacity [157].

In addition to the SnO_2 nanoparticle/graphene nanocomposites mentioned above, SnO_2 has also been engineered into various morphologies for SnO_2/graphene composites [124,151,158,159]. The hydrothermal method is one of the most widely used methods to tune SnO_2 morphologies. For example, both a flower-like SnO_2/graphene composite [160] (see Fig. 2(a)) and SnO_2 nanorods on graphene sheets [146] (see Fig. 2(b, h)) were successfully synthesized via this method. Both the flower-like SnO_2 clusters and the SnO_2 nanorods uniformly distributed on graphene sheets exhibited outstanding cycling stability and reversible discharge capacities of 730 mAh g^{-1} and 710 mAh g^{-1}, respectively. The obtained improvement is attributed to the intimate interactions between the graphene matrix and SnO_2 nanostructures, which effectively transport electrons to the current collector through the highly conducting three-dimensional graphene network [146]. GNSs in the composites provide a large contact area for dispersion of SnO_2 and act as an excellent conductive agent to provide a highway for electron transport, improving the accessible capacity [160]. X.S. Zhou et al. [161] proposed a new type of graphene-enwrapped SnO_2 hollow nanosphere composite for LIB anodes (see Fig. 2(c)). It was observed that this novel structure shows a specific capacity as high as 696 mAh g^{-1} even after 300 cycles at 0.5 A g^{-1}. The superior electrochemical performance is due to the presence of the graphene substrate and the unique structure of SnO_2, as well as the synergetic effect between graphene and SnO_2 [162]. In this system, GNSs serve as a flexible strengthening agent for the SnO_2 anode [161].

Aggregation of nanostructured SnO_2 occurs during in situ growth of SnO_2 particles on the graphene surface when using cetyltrimethylammonium bromide as the structure-directing agent; this results in decreased specific surface area and therefore decreased electrochemical performance. A mesostructured graphene-based SnO_2 composites was prepared [162] to relieve the aggregation of SnO_2 nanoparticles on the graphene surface. The obtained mesostructure can be seen in the TEM image of Fig. 2(d) and the related schematic mechanism for the formation of the composite is shown in Fig. 3(a). The presence of the GNSs matrix, the mesostructure and the synergetic effect between GNSs and mesostructure help improve electrochemical performance, leading to higher capacity and better cycling performance and rate capability (see Fig. 3(c)).

A new kind of graphene nanoribbon (GRN), which is derived from sodium/potassium unzipping of multiwall carbon nanotubes was proposed to address the problem of SnO_2 aggregation [163], as shown in Fig. 3(b). In this system, the high aspect ratio of GNRs could serve as a mechanical buffer for SnO_2 nanoparticles [163]. As a result, its reversible capacity is maintained at 825 mAh g^{-1} at 100 mA g^{-1} and 580 mAh g^{-1} at 2 A g^{-1} after 50 cycles (see Fig. 3(d)).

The high flexibility of graphene can be the perfect supporting matrix or coating layer for Sn-based materials, effectively relieving the volume expansion of SnO_2. And the beneficial synergistic effect between graphene and tin nanoparticles can further relieve the aggregation and re-stacking of SnO_2 nanoparticles. Moreover, the highly conductive graphene supplies 2D electronically conducting networks for the Sn-based materials, which further provide a highly conductive medium for Li-ion electron transfer during the charge/discharge processes.

2.3. Sn sulfide/graphene composite

Recently, various metal sulfides, especially SnS_2, have been studied as possible candidates for LIB anode materials because of their higher capacities [164–173]. Many attempts have been made to improve the electrochemical performance of SnS_2 anodes [174–178]. For example, [42] Ce was doped into 3D nanoflower-like SnS_2 by a hydrothermal route. The large-radius cerium ions can be substitutes for Sn^{4+} in the SnS_2 lattice. The expansion of the crystal lattice can provide more lattice space for lithiation process, and improves the cycling performance of Ce-doped SnS_2. Importantly, various carbon structures, such as mesoporous carbon [179] and multiwalled carbon nanotubes [180], have been used to anchor

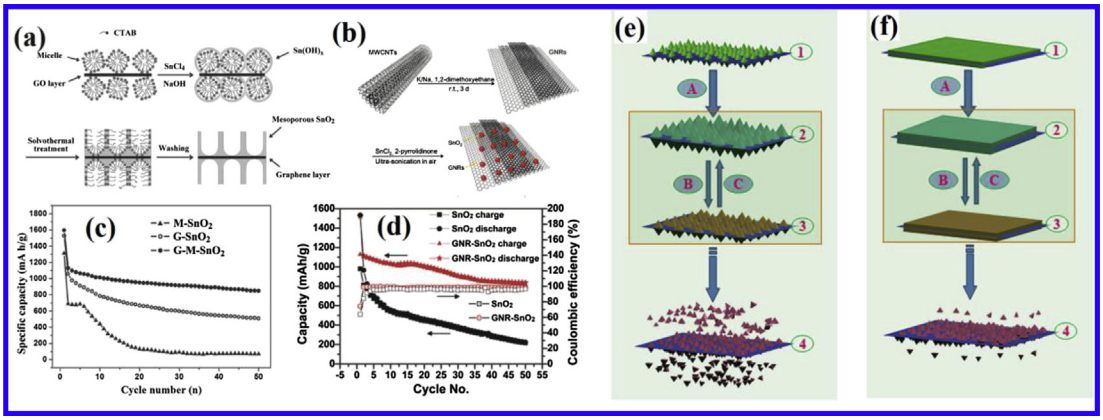

Fig. 3. Schematic mechanism for the formation (a) and the discharge capacities at 0.1 C (c) of a mesostructured graphene-based SnO_2 composite; Reproduced from Ref. [162]; schematic diagram showing the synthesis (b) and comparison of capacity retention and coulombic efficiency (d) of the GNR/SnO_2 composite; Reproduced from Ref. [114]; Morphological evolution of (e) the crystalline SnO_2-GNS and (f) the amorphous SnO_2-GNS as the nanocomposite anodes in the charge/discharge cycles; Reproduced from Ref. [119].

with SnS_2 nanosheets in order to increase the electrical conductivity of the SnS_2 anode and thereby enhance battery performance. Following this strategy, GNSs, as an excellent matrix, have been introduced to create composite anodes. GNSs combined with Ce-doped SnS_2 nanocomposites [181] show high capacity retention (707 mAh g^{-1} at 0.5 C after 50 cycles), which demonstrates that the introduction of GNSs greatly increases SnS_2 performance (446 mAh g^{-1} for Ce–SnS_2 after 50 cycles). Thus, a series of tin sulfide/graphene composites were recently reported in the literature [182–189]. The hydrothermal route is one of the most popular methods for preparing SnS_2/GNSs composites [190] and another one-step microwave-assisted technique has been attempted to synthesize these composites [182]. In these two systems, GNSs play an important role in the composites, improving the Li-storage properties. Both SnS_2/graphene composites exhibit high reversible capacities with good cycling stability and extraordinary rate capability.

A novel nanocomposite electrode material composed of micrometer-sized GNSs with a uniform distribution of ultrathin SnS_2 (~2 nm) nanoparticles [191], is shown in Fig. 4(a) and (b). This design exhibits a reversible capacity of 1002 mAh g^{-1} and charge capacity of 577 mAh g^{-1} after 50 cycles. A unique plate-on-sheet structure was studied where ultrathin SnS_2 nanoplates with a lateral size of 5–10 nm are anchored on graphene nanosheets with a preferential (001) orientation [192]. The HR-TEM and AFM images in Fig. 4(c) and (d) indicate that the SnS_2 nanoplates align on graphene with c-axis orientation. The nanohybrid exhibits a remarkably enhanced cycling stability and rate capability (see Fig. 5(a)). Both studies demonstrated that the improved electrochemical properties of these composites are due to the graphene matrix, which offers two-dimensional conductive networks and a large surface area while dispersing and immobilizing the ultrathin SnS_2 nanoplates. It also buffers the volume changes during cycling and directs the growth of SnS_2 nanoplates with a favorable orientation; this preferred orientation enhances Li-ion storage, resulting in high capacity retention and good cyclic performance [191,192].

Similar to the above Sn-based/GNSs composites, the morphologies, particle sizes and distribution of SnS_2 have apparent effects on the electrochemical performance of SnS_2/GNSs composites. It is considered that the smaller particle sizes, the thinner thickness and rational distribution can be beneficial to the properties of composites. A hybrid structure involving ultrasmall SnS_2 nanocrystals deposited on flexible RGO was proposed by L. Mei and co-workers [193]. As shown in the TEM images in Fig. 4(e) and (f), the SnS_2 nanocrystals are uniformly distributed on the RGO nanosheets, increasing the loading number of SnS_2 per unit area of the RGO matrix. Another research demonstrated a similar effect of the RGO matrix, achieving very high specific capacities with SnS_2/RGO composites, up to 1034 mAh g^{-1} after 200 cycles at 0.1 C (Fig. 5(b)) [194]. Three typical SnS_2/graphene samples with different lateral sizes of SnS_2 plates have been prepared, which demonstrated that the reversible capacity of small SnS_2 plates is stable at 650 mAh g^{-1} after 30 cycles. Interestingly, the larger SnS_2 nanoplates (G–SnS_2-L) exhibit inferior rate performance, as shown in Fig. 5(c) and (d). The Nyquist plots, shown in Fig. 5(f), are clear evidence that the graphene-containing samples possess high electrical conductivity and a fast charge-transfer reaction for lithium ion insertion and extraction, further supporting the combination of graphene and SnS_2 nanoplates [195]. Moreover, these composites exhibited excellent capacity retention at high rates for 450 cycles, maintaining capacities at 773 mAh g^{-1} and 415 mAh g^{-1} at 1 C and 5 C, respectively. The researchers reported that RGO is not only used as a solid support on which to uniformly distribute the SnS_2 nanocrystals, but also as a carrier to accelerate electron transport. Thus, SnS_2 nanocrystals deposited on RGO can increase the electrochemical capacity per unit area [193].

Anodes comprised of self-assembled graphene aerogels and composites of 2D graphene embedded with metal or metal oxide nanoparticles also exhibit improved performance [196–201]. These unique structures will provide the enhanced conductive network and more stable structure. The 3D SnS_2/graphene aerogels (SnS_2/G-A) were fabricated via a hydrothermal process [187] and then freeze-dried to maintain the 3D monolithic architectures, as shown in Fig. 4(g) and (h). The interconnected graphene networks serve as channels, enabling fast electron transport in three dimensions. The GNSs also inhibit the aggregation of SnS_2 nanoplates and act as a buffer to accommodate the volume expansion/contraction of SnS_2 during Li^+ insertion/extraction. As a result, the proposed SnS_2/graphene aerogels show high reversible capacity and excellent rate capability [187]. The schematic representation of electron transmission and lithium ion storage in SnS_2/G-A is shown in Fig. 5(e), which further explains the beneficial effects of graphene in the composites.

2.4. Stannate/graphene composites

A series of stannates, such as M_xSnO_y (M = Li, Ca, Zn, Mg, Co, Cd) [36,37,202–211], have attracted increasing attention due to their high lithium storage capacity and their ability to relieve stress arising from volume changes during cycling. This is attributed to

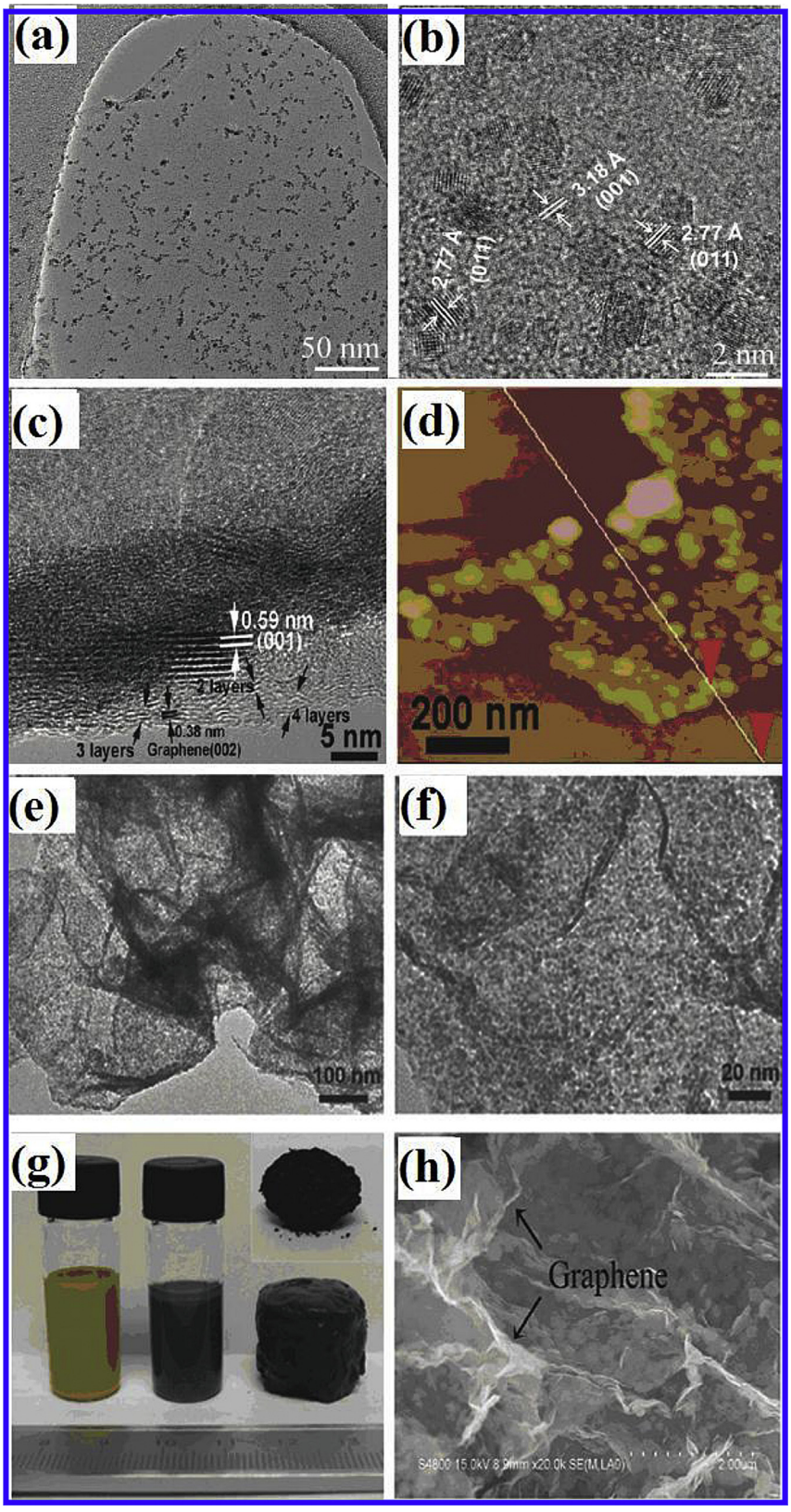

Fig. 4. HR-TEM images of the SnS_2/GNS nanocomposite (a, b); Reproduced from Ref. [191]; one stand-up sheet of SnS_2/graphene (c); Reproduced from Ref. [192]; and SnS_2 nanocrystals@RGO (e, f); Reproduced from Ref. [193]; AFM image of SnS_2/graphene (d); Reproduced from Ref. [192]; photographs of three kinds of samples: SnS_2 (left), SnS_2/G-hydrogel (middle), SnS_2/G-aerogel before freeze-drying (right), SnS_2/G-aerogel after freeze-drying (inset) (g); cross-sectional SEM image of SnS_2/G-aerogel (h); Reproduced from Ref. [187].

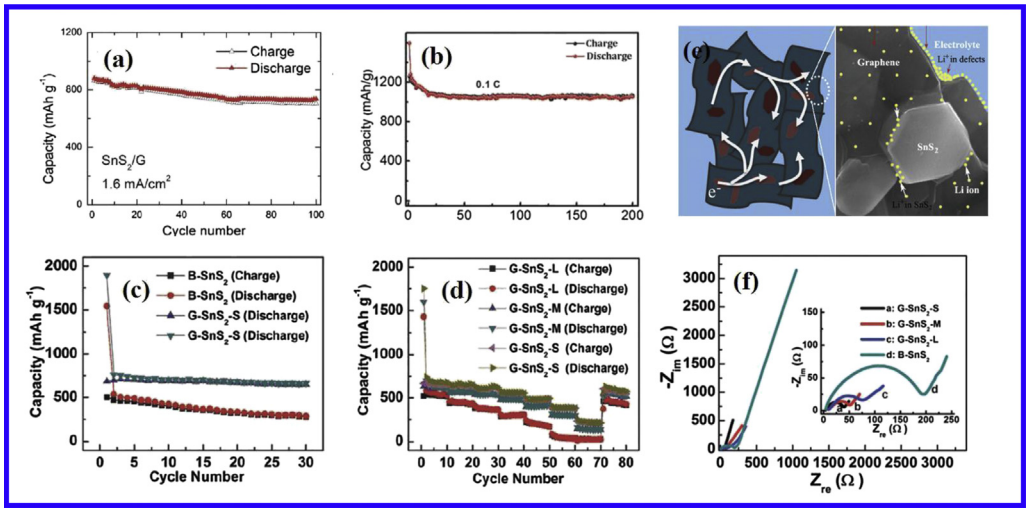

Fig. 5. Cycling stability of SnS_2/graphene and capacity retention of the composites (a); Reproduced from Ref. [192]; cycling behavior of the SnS_2 nanocrystals@RGO electrode at a rate of 0.1 C (b); Reproduced from Ref. [194]; cycling performance (c) and rate performance (d) of G–SnS_2-S, G–SnS_2-M, and G–SnS_2-L electrodes; Reproduced from Ref. [194]; schematic representation of electron transmission and lithium ion storage in SnS_2/G-A (e); Reproduced from Ref. [187]; Nyquist plots of the G–SnS_2-S, G–SnS_2-M, G–SnS_2-L and B–SnS_2 electrodes obtained by applying a sine wave with an amplitude of 5.0 mV in the frequency range from 100 kHz to 10 MHz (f).; Reproduced from Ref. [194].

the formation of electrochemically active/inactive MO_x matrices occurring during the first discharge process [209,210]. However, stannates suffer from volume expansion/contraction to some degree. Many approaches have been adopted to address these problems, such as various buffering materials made of carbon and conductive polymers [8,212–222]. Among these attempts, GNSs provide a significant improvement to the electrochemical properties of the composites. Recently, via a facile in situ solvothermal route, a $CoSnO_3$/GNS nanohybrid was designed [223]. $CoSnO_3$ nanoparticles were distributed on the surface of GNSs (see Fig. 6(c)), which supplied 2D electronically conducting networks for the nanoparticles. As a result, the composites exhibit a charge capacity as high as 649 mAh g^{-1} in the 50th cycle as well as excellent high-rate cycling stability, which is better than that of pure $CoSnO_3$ [223], demonstrating the superior advantage of using a GNS matrix in stannate anodes.

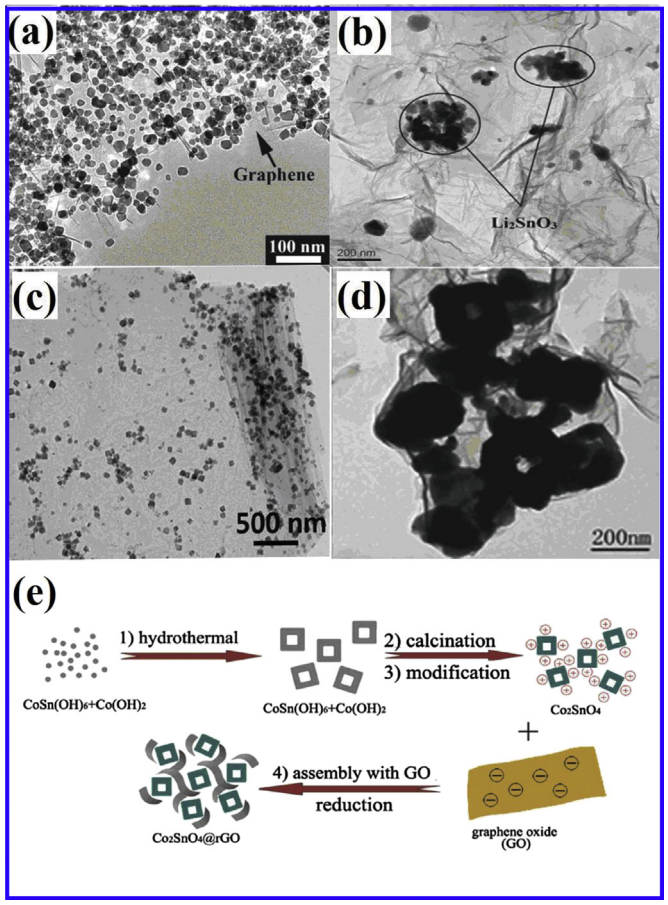

Fig. 6. TEM images of Zn_2SnO_4/G (a); Reproduced from Ref. [224]; Li_2SnO_3/graphene composites (b); Reproduced from Ref. [225]; $CoSnO_3$/graphene nanohybrids (c); Reproduced from Ref. [213]; and Co_2SnO_4 HC@rGO (d); schematic illustration of the formation of Co_2SnO_4 HC@rGO (e); Reproduced from Ref. [226].

Similarly, a layered Zn_2SnO_4/graphene nanohybrid (see Fig. 6 (a)) was synthesized via a facile in situ hydrothermal route [224]. In this anode system, the improved cycling stability is due to the buffering effect of the GNSs matrix, which effectively alleviates the large volume changes of Zn_2SnO_4 upon Li insertion/extraction. Moreover, aggregation of the nanoparticles is inhibited by the GNS matrix [224]. Our previous work also confirms this immobilization effect [225]. We found that the introduction of a GNSs matrix significantly improves the electrochemical performance of Li_2SnO_3 anodes. We proposed that the improvement results from the enhanced conductive and buffering matrix of GNSs to keep the entire composite stable. Therefore, the flexible GNS matrix acts as the supporting layers for Zn_2SnO_4 and Li_2SnO_3, which can be observed in the TEM images of Fig. 6(a) and (b).

GNSs coatings have been employed to study stannate/graphene composites via an analogous mechanism of electrostatic interactions [226]. For example, Co_2SnO_4 hollow cubes were first functionalized to give them a positively charged surface and then assembled with negatively-charged GO. The schematic illustration is shown in Fig. 6(e). The Co_2SnO_4 with GNSs coating exhibits stable cyclability (1016.2 mAh g^{-1} at 100 mA g^{-1} up to 100 cycles) and superior high-rate capability (775 mAh g^{-1} at 500 mA g^{-1}). Obviously, the GNSs coating improves not only the structural stability but also the lithium storage kinetics and electronic transport of Co_2SnO_4 [226].

Based on our previous study of Zn_2SnO_4 hollow boxes, two types of Zn_2SnO_4/graphene composites were synthesized via different methods. One approach used a simple co-precipitation and alkali etching method [227] and the other [228] used the electrostatic

interaction technique discussed above [226]. Both types of Zn_2SnO_4/graphene composites show similar morphologies, which can been observed in the TEM images of Fig. 7(a), (b), (d) and (e). The hollow Zn_2SnO_4 boxes are surrounded by the flexible GNSs. The GNSs act as the matrix for the Zn_2SnO_4 boxes, effectively buffering the volume expansion and contraction, as well as providing a highly conductive medium for electron transfer during the lithiation and de-lithiation processes [227,228]. Both of these composites demonstrate enhanced electrochemical performance and high rate capability.

In summary, for various kinds of Sn-based anodes GNSs act as a key factor for high performance binary electrodes. Table 1 summarizes the electrochemical performance of various binary composite electrodes. It is clear that the introduction of a GNSs matrix results in an improvement of the electrochemical properties. This can be attributed to the unique role of flexible GNSs, including large surface areas, good conductivity, short transportation lengths, and stress relief under large volume changes. From Table 1, one can conclude that the morphologies and structures for both Sn-based anodes and GNSs have crucial effects on the performance. Sn-based materials with small particle size, dense distribution, and unique structures, as well as GNSs with larger specific surface area should be the focus of future research to enhance LIB anode performance.

3. Sn/graphene-based ternary composites

3.1. Polymer/Sn/graphene ternary composites

Some novel ternary Sn/graphene-based composites have been developed to further enhance the performance of LIB anodes. Two types of buffering matrices, GNSs and conductive polymers, have been proposed to relieve the stress caused by volume expansion of Sn-based anodes, resulting in better cycling and rate properties. Conductive polymers, such as polyaniline (PANI), polypyrrole (PPY) and poly(3,4-ethylenedioxythiophene) (PEDOT) [229,230] provide a conductive backbone for the active materials and its soft-structured matrix can buffer the internal stress of electrodes suffering from large volume changes [231–236].

In our previous study, a new ternary graphene/Li_2SnO_3/PPY composite was designed [237], where the co-introduction of PPY and graphene created a double buffering structure for Li_2SnO_3 electrodes, achieving a reversible capacity of 699.4 mAh g^{-1} after 30 cycles. A. Bhaskar et al. [238] also studied ternary composites. They synthesized hybrids of SnO_2 hollow spheres embedded in GO and enveloped by a sheath of PEDOT, as shown in the schematic illustration of Fig. 8. These ternary composites enhanced electronic and ionic conductivity of the electrode, induced by GO and PEDOT. Furthermore, the GNSs also alleviated the mechanical stress caused by the severe volume change during lithium insertion and extraction, and reduced the detachment of electroactive material from the electrode. The buffering layer also inhibited the aggregation of tin nanoparticles. Conductive polymers, such as PANI, PEDOT and PPY, can prevent the direct contact of Sn-based crystallites with the electrolyte and thus inhibit any side chemical reactions of the electrolyte with the oxide. The coulombic efficiency of ternary hybrid for the 3rd cycle reached to 96.5% and it gradually increased with cycling. After 150 cycles the hybrid showed a reversible capacity of 608.4 mAh g^{-1} with a Coulombic efficiency more than 99%.

3.2. C/Sn/graphene ternary composites

The GNSs-Sn based binary composites were further coated with carbon as a second buffering matrix to improve the cycling performance [239–241]. Z.P. Guo's group [242] studied carbon-coated SnO_2 nanoparticle–graphene nanosheet composites. They reported that the synergy between large area GNSs and the carbon coating layer (Fig. 9(a)) alleviates the effects of volume changes, stabilizes the structure, and increases the conductivity. Thus, the composites exhibited excellent electrochemical performance with high capacity and good cycling stability (757 mA h g^{-1} after 150 cycles at 200 mA g^{-1}). We also confirmed similar effects on lithium storage using Li_2SnO_3 anodes [243]. In this double-buffering system, the obtained C/Li_2SnO_3/graphene composites also exhibited high reversible capacity and good cycling stability (736.3 mAh g^{-1} after 50 cycles at 60 mA g^{-1}).

In a previous study, we fabricated a novel sandwiched hierarchical structure composed of a graphene substrate, intermediate

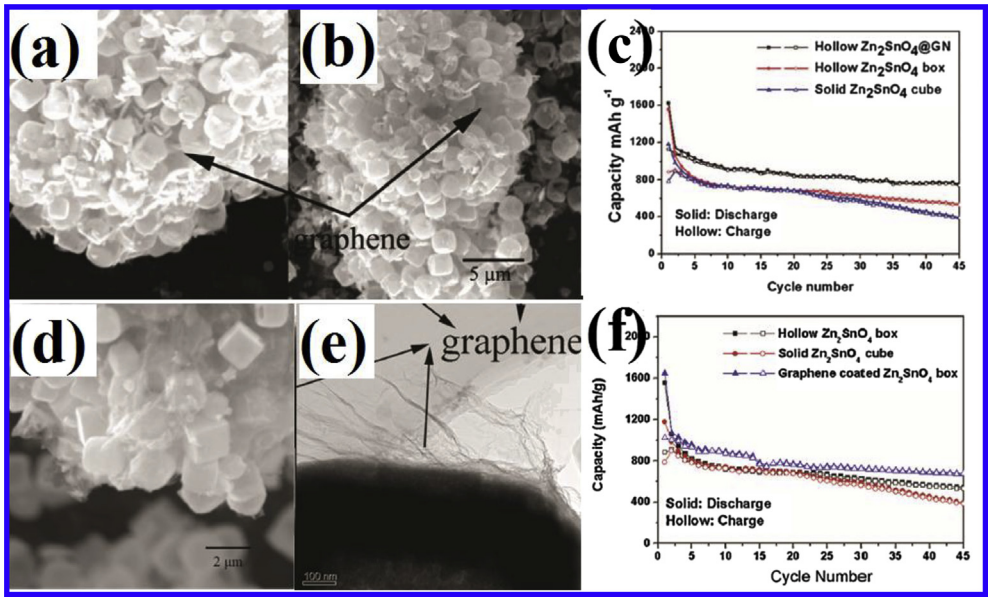

Fig. 7. TEM images of Zn_2SnO_4/graphene composites prepared via coprecipitation method (a, b) and electrostatic interactions (d, e); cycling properties of two Zn_2SnO_4/graphene composites (c, f). Reproduced from Refs. [227,228].

Table 1
Electrochemical performance of various Sn/graphene-based binary LIB electrodes.

Materials	Feature	Electrochemical performance			Ref
		Current density	Cycle number	Capacity retention	
SnO_2/graphene composites	SnO_2 nanoparticles with an average diameter of 3 nm	2 A g^{-1}	1000	1813 mAh g^{-1}	[157]
SnS_2/GNSs nanocomposites	Thicknesses of the SnS_2 plate and the graphene sheet are measured to be 2–5 nm and 1–2 nm	1.6 mA cm^{-2}	100	704 mAh g^{-1}	[192]
SnS_2/RGO nanocomposites	Plentiful SnS_2 nanocrystals deposited on flexible RGO	0.1 C	200	1034 mAh g^{-1}	[193]
Co_2SnO_4 hollow cubes@RGO nanocomposites	Co_2SnO_4 hollow cubes encapsulated in graphene	100 mA g^{-1}	100	1000 mAh g^{-1}	[226]
Hollow Zn_2SnO_4@graphene composites	Hollow boxes supported by flexible graphene sheets	300 mA g^{-1}	45	752 mAh g^{-1}	[227]
Graphene networks anchored with Sn@graphene	3D porous graphene networks anchored with Sn nanoparticles encapsulated in graphene shells	200 mA g^{-1}	340	1076 mAh g^{-1}	[117]
Graphene nanoribbons (GNRs) and tin oxide	GNRs prepared using sodium/potassium unzipping of multiwall carbon nanotubes	100 mA g^{-1}	50	825 mAh g^{-1}	[163]

SnO_2 nanorod (NR) arrays, and a carbon coating, which buffered the large volume changes experienced by the anode [244]. The synthesis procedure of the composites is illustrated in Fig. 10(a) and the novel structure of the composites can be seen in the TEM image of Fig. 9(b). Fig. 10(e) shows how the sandwiched structure prevents isolation of the SnO_2 NRs during cycling. Moreover, strong internal chemical bonding between the SnO_2 nanorods and carbon layer was discovered using spectroscopy techniques. The hierarchical sandwiched structure enhances the lithium storage properties (Fig. 10(b)) and coulombic efficiency. Encouraged by the results of the sandwiched hierarchical structure, we also designed a novel hierarchical carbon-encapsulated-tin (Sn@C) embedded GNSs composite via a simple and scalable one-step chemical vapor deposition procedure [245]. In this system, the graphene-supported Sn@C core–shell structures consist of a crystalline tin core, which is thoroughly covered by a carbon shell. Importantly, extra voids are present between the carbon shell and tin core (Fig. 9(c)). The advantages of this system are that the flexible and robust GNSs act as a support, allowing the outer carbon shell to better confine the Sn nanoparticles and improve their mechanical properties. Thus, the Sn@C–GNSs composites exhibit both excellent cycle stability and high specific capacity, in which the discharge capacity remains at 566 mAh g^{-1} after 100 cycles. A different approach has been used for ternary composites [246]: combine a simple hydrothermal method used for the synthesis of the carbon-coated SnO_2 nanocomposites with a hydrothermal self-assembly and thermal treatment used for SnO_2@C/graphene nanocomposites. The schematic illustration and TEM image of the composites are shown in Figs. 10(c) and 9(d), respectively. The composites exhibit excellent cycling stability and rate capability due to the double conductive network and buffering matrix (Fig. 10(d)). Based on the above discussion, it can be concluded that the carbon coating, combined with GNSs, creates a 3D carbon conductive network. Moreover, the carbon coating can effectively suppress the aggregation of nanoparticles and undesired side reactions. Therefore, the role of the carbon coating and GNSs as double buffering matrices dramatically enhances the electrochemical performance of Sn-based anodes [240,243,245–247].

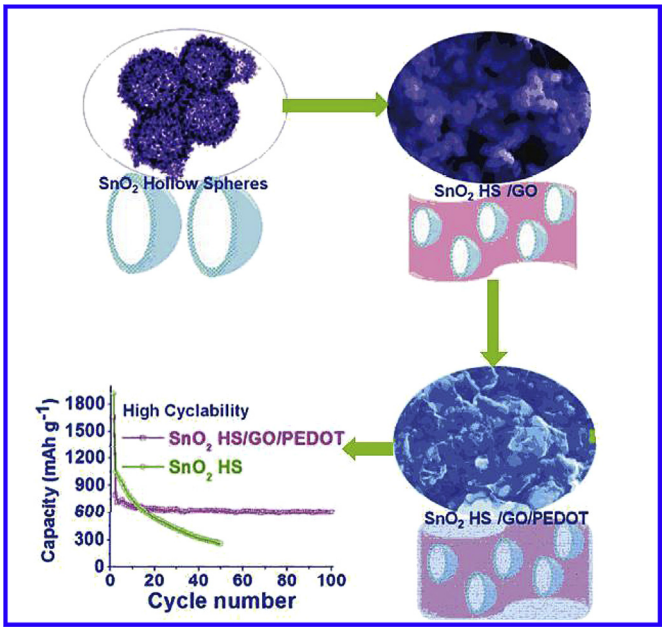

Fig. 8. Schematic representation of the formation and cycling performance of SnO_2 hollow sphere/GO/PEDOT hybrids. Reproduced from Ref. [238].

In addition to carbon coatings, other carbon materials, such as carbon nanotubes [248–250] and carbon nanofibers [251], have been introduced into the Sn/graphene-based composites. A new kind of corn-like graphene-SnO_2-carbon nanofiber mixture was developed [251] (GSCN, Fig. 9(e)) and delivered a remarkable capacity of 1246.3 mAh g^{-1} at 0.5 A g^{-1}. Fig. 10(f) shows a schematic illustration of the electronic transport route and the volume effect of GSCNs during the Li-ion insertion–extraction process. The volume expansion that occurs when Li^+ inserts into SnO_2 may be hindered by the inner carbon nanofibers (CNFs) and the outer graphene sheets. In another report, CNF has also been introduced to form the conductive network (Fig. 9(f)) [252]. In this system, carbon nanofibers and nanotubes facilitate the formation of a 3D electronic conductive network with GNSs and increase the distance between graphene layers, which provides a large number of active sites and allows for easier migration of Li-ions. This ultimately enhances the conductivity and shortens the electronic transport route [253]. As a result, the nanocomposite exhibited a highly reversible capacity and excellent rate performance.

3.3. Other graphene-based ternary composites

Besides various carbon materials, different inorganic particles of electrochemically active materials that exhibit low volume change have been introduced into Sn/graphene-based binary composites [254–258]. For example, as shown in the schematic illustration of Fig. 11(a), core–shell structured Fe_2O_3@SnO_2 nanoparticles were synthesized via a facile hydrothermal route. A flexible GO film was then covered with the spindle-like Fe_2O_3@SnO_2 nanoparticles through vacuum filtration, followed by thermal reduction [259]. The interconnected porous GNSs networks provide good electronic conductivity and a rapid electrolyte diffusion channel, as well as

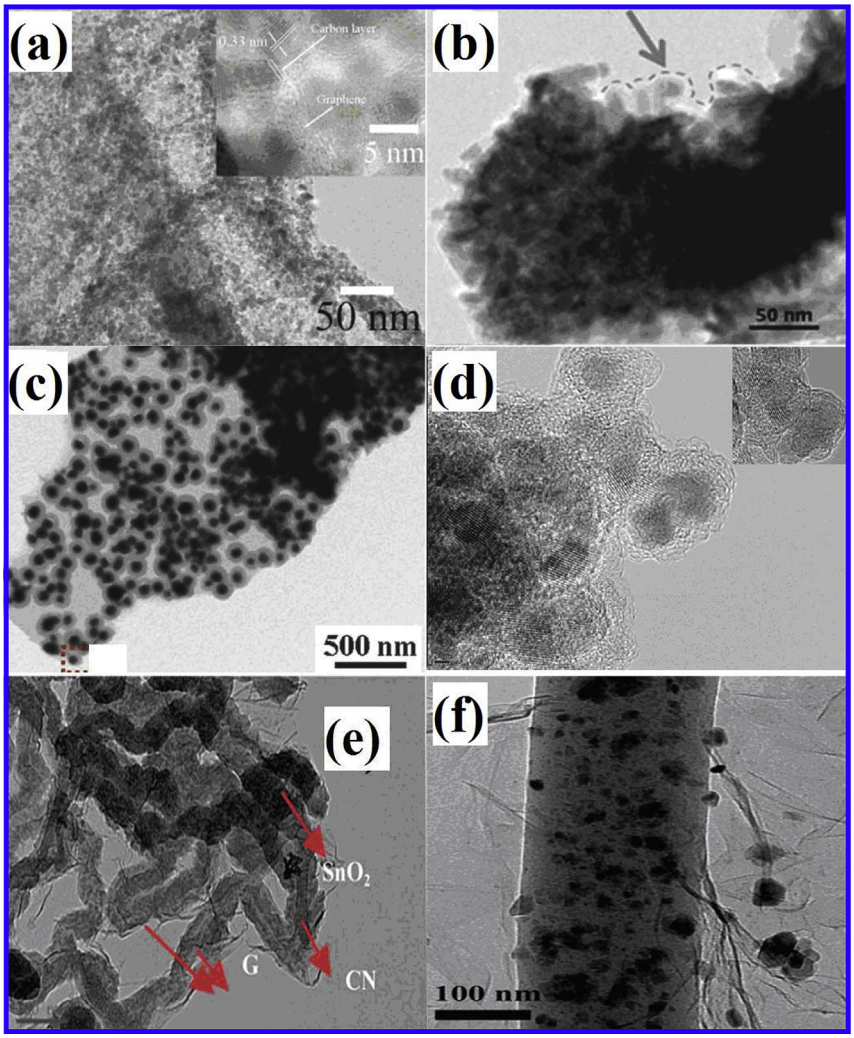

Fig. 9. TEM images of GNS–SnO_2–C (a); Reproduced from Ref. [242]; GNS/SnO_2 NR/C (b); Reproduced from Ref. [244]; Sn@C–GNS (c); Reproduced from Ref. [245]; SnO_2@C/graphene (d); Reproduced from Refs. [246]; graphene–SnO_2–carbon nanofiber mixture (e) and SnO_x@carbon nanofibers (f); Reproduced from Refs. [251,252].

aids the Fe_2O_3 and SnO_2 in retarding electrochemical aggregation of the nanoparticles [259]. A similar system with graphene–TiO_2–SnO_2 ternary nanocomposites (GTS) also examined these effects. In this case, TiO_2 and SnO_2 nanoparticles were formed in situ and uniformly anchored on the surface of reduced graphene oxide sheets (see Fig. 11(c)) [260]. Here, the contribution of anatase TiO_2 to the total specific capacity of the obtained ternary nanocomposites is limited by its low theoretical specific capacity. However, the small amount of TiO_2 nanoparticles creates more space to accommodate the electrode volume change and acts as a stable barrier to effectively prevent the agglomeration of SnO_2 nanoparticles during the charge–discharge process [260]. Therefore, the as-synthesized ternary GTS nanocomposites delivered improved cycling performance (537 mA h g^{-1} at 50 mA g^{-1} with a coulombic efficiency of 97% after 50 cycles) and good reversible capacities (250 mA h g^{-1} even at a current density of 1000 mA g^{-1}) (Fig. 11(d)).

4. Doped graphene/Sn composite

In all of the above discussions, we mainly reviewed the effect of pristine GNSs on lithium storage for Sn-based composite anodes. It has been reported that graphene doped with heteroatoms can be tailored in terms of its electronic properties and chemical reactivity. Heteroatom doping of graphene can aid in the formation of strong bonds between the graphene support and Sn-based particles via a charge transfer mechanism [261]. Moreover, doped graphene acts as an effective conductive additive and reduces the electrolyte decomposition at the dangling edges of the graphene structure [82,261,262]. Thus, in the case of Sn-based anode materials, the doping behavior of GNSs matrices has an important influence on lithium storage. The doped graphene/Sn composites always exhibit a large capacity, high rate capability, and excellent cycling stability [261,263–265]. For instance, Y.Y Guo et al. [266] reported N-doped GNS-SnO_2 sandwich papers with 7,7,8,8-tetracyanoquinodimethane anions. Another SnO_2 NC@N-RGO hybrid material prepared via in situ hydrazine monohydrate vapor reduction with a stable capacity of 1346 mAh g^{-1} after 500 cycles has been reported [267]. 3D macroscopic tin oxide/nitrogen-doped graphene frameworks (SnO_2/N-GN) were constructed by a novel solvothermal-induced self-assembly process, using a SnO_2 colloid as a precursor [268]. The optimized electrode has a N-GNS content of 44.23% and exhibited superior rate capability (1126, 855, and 614 mAh g^{-1} at 1000, 3000, and 6000 mA g^{-1}, respectively), as well as extraordinary prolonged cycling stability at high current densities (905 mAh g^{-1} after 1000 cycles at 2000 mA g^{-1}). It was found that

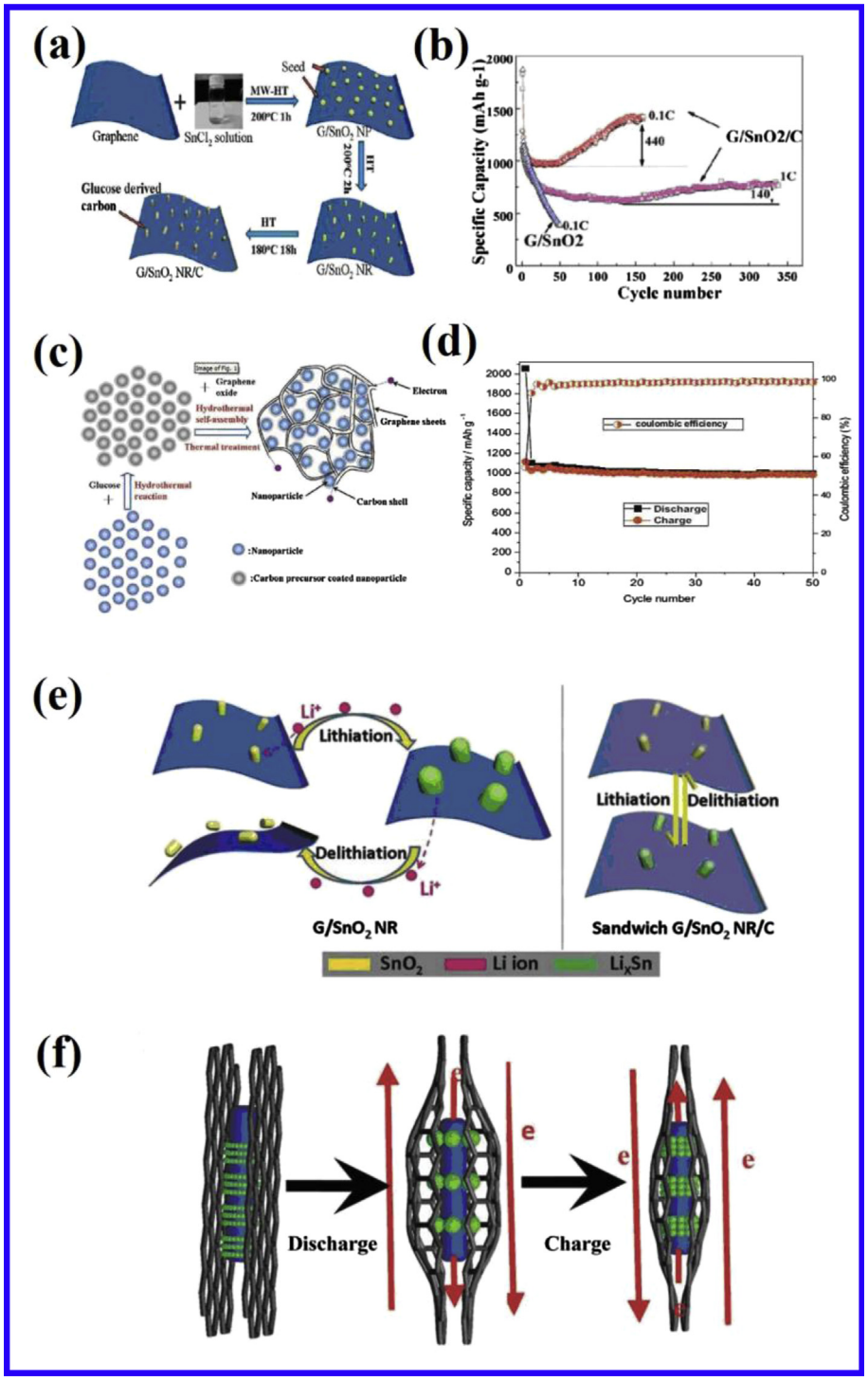

Fig. 10. Illustration of the synthesis process (a) and cycling performance (b) of G/SnO_2 NR/C nanocomposites; Reproduced from Ref. [244]; schematic illustration (c) and capacities versus cycle number (d) of SnO_2@C/graphene nanocomposite; Reproduced from Ref. [246]; schematic representation showing that the sandwiched structure prevents isolation of SnO_2 NRs during cycling (e); Reproduced from Ref. [246]; schematic illustration of the volume change for GSCN during the Li-ion insertion–extraction process (f); Reproduced from Ref. [244].

the formation of Sn–N bonds between SnO_2 nanocrystals and GNSs effectively mounted SnO_2 nanocrystals onto the matrix, thus suppressing the aggregation of Sn nanoparticles during the lithiation process. In addition, the undisturbed electron supply from N-RGO enhanced the electrochemical activity of the SnO_2 nanocrystals, resulting in improved reversibility of the SnO_2 conversion reaction [267].

5. Summary and perspective

We have reviewed the recent research on the effects of GNSs for high performance Sn-based anodes and summarized the preparation, structure, and electrochemical properties of different Sn/graphene-based composites. Table 2 shows the electrochemical performance for different kinds of Sn/graphene-based LIB

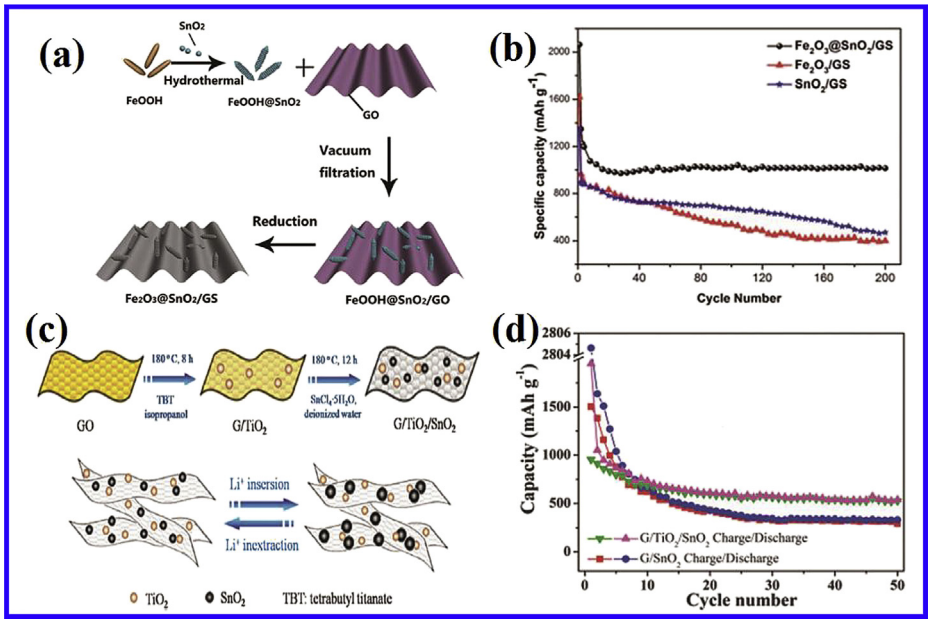

Fig. 11. Schematic illustration (a) and cycling performance (b) of the Fe_2O_3@SnO_2/GS films; Reproduced from Refs. [259]; synthesis steps and structure of GTS ternary nanocomposites (c); comparison of charge–discharge cycling performance of GNS and GTS electrodes at a current density of 50 mA g^{-1} (d); Reproduced from Ref. [260].

electrodes. In these composites, GNSs always provide remarkable advantages for Sn-based anodes, which can be attributed to the unique structure and properties of GNSs, such as high surface area, electrical conductivity, mechanical flexibility, and chemical functionality. Thus, as one excellent matrix, GNSs play an important role in the composites, drastically improving the lithium storage performance of Sn-based anodes.

The significant effects of GNSs on high performance Sn-based anodes can be summarized as follows: (1) Its high flexibility makes graphene the perfect supporting matrix or coating layer for Sn-based materials, effectively relieving the main problem of Sn-based anodes: volume expansion. (2) Layered GNSs inhibit the aggregation of Sn-based particles. Sn-based particles between graphene layers efficiently suppress the re-stacking of graphene. There is a beneficial synergistic effect between graphene and tin nanoparticles. (3) The highly conductive graphene supplies 2D electronically conducting networks for the Sn-based materials, which further provides a highly conductive medium for Li-ion electron transfer during the charge/discharge processes. (4) The oxygen-rich functional groups on the surface of graphene or graphene oxide can serve as good interfacial interactions for the growth of various Sn-based materials. Due to these properties, Sn/graphene-based composites exhibit excellent electrochemical performance as anode materials for LIBs.

As discussed, many achievements have been obtained using a GNS matrix to improve the battery performance of Sn-based composite anodes. However, some challenges still limit the commercialization of Sn-based anodes. On one hand, one of the most important problems is the large-scale, low cost and simple production of high quality GNSs. On the other hand, in order to improve the performance of the Sn-based anodes, controlled synthesis of Sn/graphene-based materials should be further explored, including the distribution, density, chemical bonding, and three dimensional arrangements of the composites [117]. The design of Sn/graphene-based structures, including alternative stable materials such as carbon coatings, carbon nanofibers or nanotubes,

Table 2
Electrochemical performance of Sn/graphene-based LIB electrodes.

Type of materials	Materials	Synthesis method	Electrochemical performance			Ref
			Current density	Cycle number	Capacity retention	
Sn binary composite	Sn/graphene composite	Microwave reduction	100 mA g^{-1}	100	500 mAh g^{-1}	[111]
Sn binary composite	Sn nanopillar arrays embedded between GNS	Film deposition and annealing process	0.5 A g^{-1}	40	508 mAh g^{-1}	[10]
SnO_2 binary composite	SnO_2 nanorod/graphene composite	Facile electrospinning and sedimentation separation processes	100 mA g^{-1}	50	467 mAh g^{-1}	[151]
Stannate binary composite	Zn_2SnO_4/graphene nanohybrid	Hydrothermal route	200 mA g^{-1}	50	688 mAh g^{-1}	[224]
stannate binary composite	Graphene-supported Li_2SnO_3 nanocomposites	Deoxidation technique	60 mA g^{-1}	50	582.2 mAh g^{-1}	[225]
Sn ternary composite	Sn@C–GNS	CVD procedure	75 mA g^{-1}	100	566 mAh g^{-1}	[245]
SnO_2 ternary composite	Carbon coated SnO_2 NRs grafted on graphene composites	Hydrothermal growth and glucose derived	3000 mA g^{-1}	150	1419 mAh g^{-1}	[244]
SnO_2 ternary composite	Carbon-coated SnO_2 nanoparticle–GNS	Hydrothermal route	200 mA g^{-1}	150	757 mAh g^{-1}	[242]
Stannate ternary composite	Carbon-doped Li_2SnO_3/graphene composites	Hydrothermal route	60 mA g^{-1}	50	736.3 mAh g^{-1}	[243]
Doped graphene	SnO_2/N-GN hybrid	Solvothermal-induced self-assembly process	2000 mA g^{-1}	1000	905 mAh g^{-1}	[268]
Doped graphene	Co_3Sn_2@Co nanoparticles and nitrogen-doped graphene	Hydrothermal synthesis, followed by annealing process	250 mA g^{-1}	100	1615 mAh g^{-1}	[270]

conductive polymers and other inorganic particles, is essential for forming a conductive network and double buffering matrices to effectively alleviate volume changes and stabilize the electrodes. This opens a potential approach for improving the performance of Sn-based anodes. Doping the GNS matrix with different elements (N, S, Se, P, B) is another strategy for increasing the electrochemical performance of the Sn-based anodes. In addition, Sn/graphene-based materials have the unique properties of being ultrathin, lightweight and flexible, making the fabrication of light, high energy-dense, and flexible electrodes possible [269]. GNSs clearly improve the performance and stability of Sn-based anodes. However, graphene-modified Sn-based anodes are still a new research topic, and further studies are required. With rational and careful design, Sn/graphene-based anodes will become a top candidate for next-generation LIBs.

Acknowledgments

This research was supported by Key Project of Tianjin Municipal Natural Science Foundation of China (14JCZDJC32200 and 13JCZDJC33900), National Natural Science Foundation of China (51472180 and 51272176), LPMT, CAEP (KF14006 and ZZ13007), Project 2013A030214 supported by CAEP, Science & Technology Department of Sichuan Province (2013GZX0145-3), and the program of Thousand Youth Talents in Tianjin of China.

References

[1] J.-M. Tarascon, M. Armand, Nature 414 (2001) 359–367.
[2] P. Poizot, S. Laruelle, S. Grugeon, L. Dupont, J. Tarascon, Nature 407 (2000) 496–499.
[3] M.S. Whittingham, Chem. Rev. 104 (2004) 4271–4302.
[4] Y.-K. Sun, S.-T. Myung, B.-C. Park, J. Prakash, I. Belharouak, K. Amine, Nat. Mater. 8 (2009) 320–324.
[5] M. Armand, J.-M. Tarascon, Nature 451 (2008) 652–657.
[6] J. Xie, X. Yang, S. Zhou, D. Wang, ACS Nano 5 (2011) 9225–9231.
[7] A.S. Aricò, P. Bruce, B. Scrosati, J.-M. Tarascon, W. Van Schalkwijk, Nat. Mater. 4 (2005) 366–377.
[8] Z. Wang, Z. Wang, W. Liu, W. Xiao, X.W.D. Lou, Energy Environ. Sci. 6 (2013) 87–91.
[9] C. Masarapu, V. Subramanian, H. Zhu, B. Wei, Adv. Funct. Mater. 19 (2009) 1008–1014.
[10] L. Ji, Z. Tan, T. Kuykendall, E.J. An, Y. Fu, V. Battaglia, Y. Zhang, Energy Environ. Sci. 4 (2011) 3611.
[11] E. Peled, C. Menachem, D. Bar-Tow, A. Melman, J. Electrochem. Soc. 143 (1996) L4–L7.
[12] Y. Hu, W. Kong, H. Li, X. Huang, L. Chen, Electrochem. Commun. 6 (2004) 126–131.
[13] R. Freeman, T. Finder, I. Willner, Angew. Chem. Int. Ed. 48 (2009) 7818–7821.
[14] M. Winter, G.H. Wrodnigg, J.O. Besenhard, W. Biberacher, P. Novák, J. Electrochem. Soc. 147 (2000) 2427–2431.
[15] W.M. Zhang, J.S. Hu, Y.G. Guo, S.F. Zheng, L.S. Zhong, W.G. Song, L.J. Wan, Adv. Mater. 20 (2008) 1160–1165.
[16] B. Peng, J. Chen, Coord. Chem. Rev. 253 (2009) 2805–2813.
[17] S. Yang, P.Y. Zavalij, M.S. Whittingham, Electrochem. Commun. 5 (2003) 587–590.
[18] M. Inaba, T. Uno, A. Tasaka, J. Power Sources 146 (2005) 473–477.
[19] M. Winter, J.O. Besenhard, Electrochim. Acta 45 (1999) 31–50.
[20] I.A. Courtney, J. Dahn, J. Electrochem. Soc. 144 (1997) 2045–2052.
[21] G. Derrien, J. Hassoun, S. Panero, B. Scrosati, Adv. Mater. 19 (2007) 2336–2340.
[22] B. Veeraraghavan, A. Durairajan, B. Haran, B. Popov, R. Guidotti, J. Electrochem. Soc. 149 (2002) A675–A681.
[23] J. Wang, X. Sun, Energy Environ. Sci. 5 (2012) 5163–5185.
[24] T. Zheng, W. McKinnon, J. Dahn, J. Electrochem. Soc. 143 (1996) 2137–2145.
[25] I. Meschini, F. Nobili, M. Mancini, R. Marassi, R. Tossici, A. Savoini, M.L. Focarete, F. Croce, J. Power Sources 226 (2013) 241–248.
[26] L. Ji, Z. Lin, M. Alcoutlabi, X. Zhang, Energy Environ. Sci. 4 (2011) 2682–2699.
[27] P.G. Bruce, B. Scrosati, J.M. Tarascon, Angew. Chem. Int. Ed. 47 (2008) 2930–2946.
[28] X.W.D. Lou, L.A. Archer, Z. Yang, Adv. Mater. 20 (2008) 3987–4019.
[29] M.S. Park, G.X. Wang, Y.M. Kang, D. Wexler, S.X. Dou, H.K. Liu, Angew. Chem. 119 (2007) 764–767.
[30] P. Meduri, C. Pendyala, V. Kumar, G.U. Sumanasekera, M.K. Sunkara, Nano Lett. 9 (2009) 612–616.
[31] S. Ding, J.S. Chen, G. Qi, X. Duan, Z. Wang, E.P. Giannelis, L.A. Archer, X.W. Lou, J. Am. Chem. Soc. 133 (2010) 21–23.
[32] S. Ding, X.W.D. Lou, Nanoscale 3 (2011) 3586–3588.
[33] J. Ye, H. Zhang, R. Yang, X. Li, L. Qi, Small 6 (2010) 296–306.
[34] Y. Wang, J.Y. Lee, H.C. Zeng, Chem. Mater. 17 (2005) 3899–3903.
[35] Y. Wang, H.C. Zeng, J.Y. Lee, Adv. Mater. 18 (2006) 645–649.
[36] Y. Zhao, Y. Huang, Q. Wang, K. Wang, M. Zong, L. Wang, W. Zhang, X. Sun, RSC Adv. 3 (2013) 14480–14485.
[37] Z. Wang, Z. Wang, H. Wu, X.W.D. Lou, Sci. Rep. 3 (2013).
[38] X.W. Lou, Y. Wang, C. Yuan, J.Y. Lee, L.A. Archer, Adv. Mater. 18 (2006) 2325–2329.
[39] L. Zhang, H.B. Wu, B. Liu, X.W.D. Lou, Energy Environ. Sci. 7 (2014) 1013–1017.
[40] X.W. Lou, C.M. Li, L.A. Archer, Adv. Mater. 21 (2009) 2536–2539.
[41] Z. Wang, D. Luan, F.Y.C. Boey, X.W. Lou, J. Am. Chem. Soc. 133 (2011) 4738–4741.
[42] Q. Wang, Y. Huang, J. Miao, Y. Zhao, Y. Wang, Electrochim. Acta 93 (2013) 120–130.
[43] F. Vicent, E. Morallo, C. Quijada, J. Va, A. Aldaz, F. Cases, J. Appl. Electrochem. 28 (1998) 607–612.
[44] S. Chen, P. Bao, X. Huang, B. Sun, G. Wang, Nano Res. 7 (2013) 85–94.
[45] H. Qiao, J. Li, J. Fu, D. Kumar, Q. Wei, Y. Cai, F. Huang, ACS Appl. Mater. Interfaces 3 (2011) 3704–3708.
[46] Y. Wang, I. Djerdj, B. Smarsly, M. Antonietti, Chem. Mater. 21 (2009) 3202–3209.
[47] X.W. Lou, D. Deng, J.Y. Lee, L.A. Archer, Chem. Mater. 20 (2008) 6562–6566.
[48] X.W. Lou, J.S. Chen, P. Chen, L.A. Archer, Chem. Mater. 21 (2009) 2868–2874.
[49] X. Li, Y. Zhong, M. Cai, M.P. Balogh, D. Wang, Y. Zhang, R. Li, X. Sun, Electrochim. Acta 89 (2013) 387–393.
[50] X. Li, A. Dhanabalan, L. Gu, C. Wang, Adv. Energy Mater. 2 (2012) 238–244.
[51] A.K. Geim, Science 324 (2009) 1530–1534.
[52] A. Ferrari, J. Meyer, V. Scardaci, C. Casiraghi, M. Lazzeri, F. Mauri, S. Piscanec, D. Jiang, K. Novoselov, S. Roth, Phys. Rev. Lett. 97 (2006) 187401.
[53] A.K. Geim, K.S. Novoselov, Nat. Mater. 6 (2007) 183–191.
[54] H. Gwon, H.-S. Kim, K.U. Lee, D.-H. Seo, Y.C. Park, Y.-S. Lee, B.T. Ahn, K. Kang, Energy Environ. Sci. 4 (2011) 1277–1283.
[55] D. Li, M.B. Müller, S. Gilje, R.B. Kaner, G.G. Wallace, Nat. Nanotechnol. 3 (2008) 101–105.
[56] K. Novoselov, A.K. Geim, S. Morozov, D. Jiang, M. Katsnelson, I. Grigorieva, S. Dubonos, A. Firsov, Nature 438 (2005) 197–200.
[57] S. Stankovich, D.A. Dikin, G.H. Dommett, K.M. Kohlhaas, E.J. Zimney, E.A. Stach, R.D. Piner, S.T. Nguyen, R.S. Ruoff, Nature 442 (2006) 282–286.
[58] Y. Zhu, S. Murali, W. Cai, X. Li, J.W. Suk, J.R. Potts, R.S. Ruoff, Adv. Mater. 22 (2010) 3906–3924.
[59] C. Xu, B. Xu, Y. Gu, Z. Xiong, J. Sun, X. Zhao, Energy Environ. Sci. 6 (2013) 1388–1414.
[60] C. Lee, X. Wei, J.W. Kysar, J. Hone, Science 321 (2008) 385–388.
[61] X. Huang, Z. Yin, S. Wu, X. Qi, Q. He, Q. Zhang, Q. Yan, F. Boey, H. Zhang, Small 7 (2011) 1876–1902.
[62] D.A. Dikin, S. Stankovich, E.J. Zimney, R.D. Piner, G.H. Dommett, G. Evmenenko, S.T. Nguyen, R.S. Ruoff, Nature 448 (2007) 457–460.
[63] C. Wang, D. Li, C.O. Too, G.G. Wallace, Chem. Mater. 21 (2009) 2604–2606.
[64] G. Wang, X. Shen, J. Yao, J. Park, Carbon 47 (2009) 2049–2053.
[65] P. Guo, H. Song, X. Chen, Electrochem. Commun. 11 (2009) 1320–1324.
[66] H. Xiang, Z. Li, K. Xie, J. Jiang, J. Chen, P. Lian, J. Wu, Y. Yu, H. Wang, Rsc Adv. 2 (2012) 6792–6799.
[67] M. Liang, L. Zhi, J. Mater. Chem. 19 (2009) 5871–5878.
[68] J. Hou, Y. Shao, M.W. Ellis, R.B. Moore, B. Yi, Phys. Chem. Chem. Phys. 13 (2011) 15384–15402.
[69] P. Lian, X. Zhu, S. Liang, Z. Li, W. Yang, H. Wang, Electrochim. Acta 55 (2010) 3909–3914.
[70] A. Shanmugharaj, W. Choi, C. Lee, S.H. Ryu, J. Power Sources 196 (2011) 10249–10253.
[71] L.-Z. Bai, D.-L. Zhao, T.-M. Zhang, W.-G. Xie, J.-M. Zhang, Z.-M. Shen, Electrochim. Acta 107 (2013) 555–561.
[72] Y. Fang, Y. Lv, R. Che, H. Wu, X. Zhang, D. Gu, G. Zheng, D. Zhao, J. Am. Chem. Soc. 135 (2013) 1524–1530.
[73] D. Pan, S. Wang, B. Zhao, M. Wu, H. Zhang, Y. Wang, Z. Jiao, Chem. Mater. 21 (2009) 3136–3142.
[74] A. Gerouki, M. Goldner, R. Goldner, T. Haas, T. Liu, S. Slaven, J. Electrochem. Soc. 143 (1996) L262–L263.
[75] X. Jia, J. Campos-Delgado, M. Terrones, V. Meunier, M.S. Dresselhaus, Nanoscale 3 (2011) 86–95.
[76] S.-L. Chou, J.-Z. Wang, M. Choucair, H.-K. Liu, J.A. Stride, S.-X. Dou, Electrochem. Commun. 12 (2010) 303–306.
[77] X. Li, Y. Hu, J. Liu, A. Lushington, R. Li, X. Sun, Nanoscale 5 (2013) 12607–12615.
[78] S.-L. Kuo, W.-R. Liu, C.-P. Kuo, N.-L. Wu, H.-C. Wu, J. Power Sources 244 (2013) 552–556.
[79] L.L. Zhang, X. Zhao, H. Ji, M.D. Stoller, L. Lai, S. Murali, S. Mcdonnell, B. Cleveger, R.M. Wallace, R.S. Ruoff, Energy Environ. Sci. 5 (2012) 9618–9625.
[80] S. Yang, L. Zhi, K. Tang, X. Feng, J. Maier, K. Müllen, Adv. Funct. Mater. 22 (2012) 3634–3640.
[81] D. Wei, Y. Liu, Y. Wang, H. Zhang, L. Huang, G. Yu, Nano Lett. 9 (2009) 1752–1758.

[82] X. Wang, X. Cao, L. Bourgeois, H. Guan, S. Chen, Y. Zhong, D.M. Tang, H. Li, T. Zhai, L. Li, Adv. Funct. Mater. 22 (2012) 2682–2690.
[83] H. Wang, C. Zhang, Z. Liu, L. Wang, P. Han, H. Xu, K. Zhang, S. Dong, J. Yao, G. Cui, J. Mater. Chem. 21 (2011) 5430–5434.
[84] H. Wang, T. Maiyalagan, X. Wang, Acs Catal. 2 (2012) 781–794.
[85] Y. Shao, S. Zhang, M.H. Engelhard, G. Li, G. Shao, Y. Wang, J. Liu, I.A. Aksay, Y. Lin, J. Mater. Chem. 20 (2010) 7491–7496.
[86] A.L.M. Reddy, A. Srivastava, S.R. Gowda, H. Gullapalli, M. Dubey, P.M. Ajayan, ACS Nano 4 (2010) 6337–6342.
[87] L. Panchakarla, K. Subrahmanyam, S. Saha, A. Govindaraj, H. Krishnamurthy, U. Waghmare, C. Rao, Adv. Mater. 21 (2009) 4726–4730.
[88] X. Li, D. Geng, Y. Zhang, X. Meng, R. Li, X. Sun, Electrochem. Commun. 13 (2011) 822–825.
[89] Z.-S. Wu, W. Ren, L. Xu, F. Li, H.-M. Cheng, ACS Nano 5 (2011) 5463–5471.
[90] L. Zhan, S. Yang, Y. Wang, Y. Wang, L. Ling, X. Feng, Adv. Mater. Interfaces (2014), http://dx.doi.org/10.1002/admi.201300149.
[91] C. Ma, X. Shao, D. Cao, J. Mater. Chem. 22 (2012) 8911–8915.
[92] X. Li, J. Liu, Y. Zhang, Y. Li, H. Liu, X. Meng, J. Yang, D. Geng, D. Wang, R. Li, J. Power Sources 197 (2012) 238–245.
[93] A. Ambrosi, A. Bonanni, M. Pumera, Nanoscale 3 (2011) 2256–2260.
[94] F. Liu, S. Song, D. Xue, H. Zhang, Adv. Mater. 24 (2012) 1089–1094.
[95] X. Li, J. Yang, Y. Hu, J. Wang, Y. Li, M. Cai, R. Li, X. Sun, J. Mater. Chem. 22 (2012) 18847–18853.
[96] G. Ning, C. Xu, Y. Cao, X. Zhu, Z. Jiang, Z. Fan, W. Qian, F. Wei, J. Gao, J. Mater. Chem. A 1 (2013) 408–414.
[97] Y. Hu, X. Li, D. Geng, M. Cai, R. Li, X. Sun, Electrochim. Acta 91 (2013) 227–233.
[98] Y. Hu, X. Li, J. Wang, R. Li, X. Sun, J. Power Sources 237 (2013) 41–46.
[99] C. Zhong, J.-Z. Wang, D. Wexler, H.-K. Liu, Carbon 66 (2014) 637–645.
[100] G. Fang, S. Kaneko, W. Liu, B. Xia, H. Sun, R. Zhang, J. Zheng, D. Li, Electrochim. Acta 111 (2013) 627–634.
[101] G. Wang, B. Wang, X. Wang, J. Park, S. Dou, H. Ahn, K. Kim, J. Mater. Chem. 19 (2009) 8378–8384.
[102] J. Yao, X. Shen, B. Wang, H. Liu, G. Wang, Electrochem. Commun. 11 (2009) 1849–1852.
[103] X. Wang, X. Zhou, K. Yao, J. Zhang, Z. Liu, Carbon 49 (2011) 133–139.
[104] S. Chen, P. Chen, M. Wu, D. Pan, Y. Wang, Electrochem. Commun. 12 (2010) 1302–1306.
[105] H. Kim, S.-W. Kim, Y.-U. Park, H. Gwon, D.-H. Seo, Y. Kim, K. Kang, Nano Res. 3 (2010) 813–821.
[106] Z. Wen, S. Cui, H. Kim, S. Mao, K. Yu, G. Lu, H. Pu, O. Mao, J. Chen, J. Mater. Chem. 22 (2012) 3300.
[107] L.-S. Zhang, L.-Y. Jiang, H.-J. Yan, W.D. Wang, W. Wang, W.-G. Song, Y.-G. Guo, L.-J. Wan, J. Mater. Chem. 20 (2010) 5462–5467.
[108] P. Lian, X. Zhu, S. Liang, Z. Li, W. Yang, H. Wang, Electrochim. Acta 56 (2011) 4532–4539.
[109] C. Wang, Y. Li, Y.S. Chui, Q.H. Wu, X. Chen, W. Zhang, Nanoscale 5 (2013) 10599–10604.
[110] W. Yue, S. Yang, Y. Ren, X. Yang, Electrochim. Acta 92 (2013) 412–420.
[111] F.R. Beck, R. Epur, D. Hong, A. Manivannan, P.N. Kumta, Electrochim. Acta 127 (2014) 299–306.
[112] X. Zhou, Y. Zou, J. Yang, J. Power Sources 253 (2014) 287–293.
[113] S. Chen, Y. Wang, H. Ahn, G. Wang, J. Power Sources 216 (2012) 22–27.
[114] H. Li, X. Huang, L. Chen, J. Power Sources 81 (1999) 340–345.
[115] C. Kim, M. Noh, M. Choi, J. Cho, B. Park, Chem. Mater. 17 (2005) 3297–3301.
[116] A. Jahel, C.M. Ghimbeu, L. Monconduit, C. Vix-Guterl, Adv. Energy Mater. (2014), http://dx.doi.org/10.1002/aenm.201400025.
[117] J. Qin, C. He, N. Zhao, Z. Wang, C. Shi, E.-Z. Liu, J. Li, ACS Nano 8 (2014) 1728–1738.
[118] E. Kim, D. Son, T.G. Kim, J. Cho, B. Park, K.S. Ryu, S.H. Chang, Angew. Chem. 116 (2004) 6113–6116.
[119] X. Li, X. Meng, J. Liu, D. Geng, Y. Zhang, M.N. Banis, Y. Li, J. Yang, R. Li, X. Sun, M. Cai, M.W. Verbrugge, Adv. Funct. Mater. 22 (2012) 1647–1654.
[120] H. Huang, C. Ong, J. Guo, T. White, M. Tse, O. Tan, Nanoscale 2 (2010) 1203–1207.
[121] V. Kumar, J.H. Kim, C. Pendyala, B. Chernomordik, M.K. Sunkara, J. Phys. Chem. C 112 (2008) 17750–17754.
[122] H. Li, H. Ma, Y. Zeng, A. Pan, Q. Zhang, H. Yu, T. Wang, Y. Wang, B. Zou, J. Phys. Chem. C 114 (2010) 1844–1848.
[123] N. Du, H. Zhang, B. Chen, X. Ma, D. Yang, Chem. Commun. (2008) 3028–3030.
[124] S. Ding, D. Luan, F.Y.C. Boey, J.S. Chen, X.W.D. Lou, Chem. Commun. 47 (2011) 7155–7157.
[125] Y. Li, Y. Guo, R. Tan, P. Cui, Y. Li, W. Song, Mater. Lett. 63 (2009) 2085–2088.
[126] C. Wang, G. Du, K. Ståhl, H. Huang, Y. Zhong, J. Jiang, J. Phys. Chem. C 116 (2012) 4000–4011.
[127] H.B. Wu, J.S. Chen, X.W. Lou, H.H. Hng, J. Phys. Chem. C 115 (2011) 24605–24610.
[128] R. Yang, Y. Gu, Y. Li, J. Zheng, X. Li, Acta Mater. 58 (2010) 866–874.
[129] X.W. Lou, C. Yuan, L.A. Archer, Small 3 (2007) 261–265.
[130] X.W. Lou, C. Yuan, L.A. Archer, Adv. Mater. 19 (2007) 3328–3332.
[131] L. Zhang, G. Zhang, H.B. Wu, L. Yu, X.W.D. Lou, Adv. Mater. 25 (2013) 2589–2593.
[132] G. Zhou, D.-W. Wang, L. Li, N. Li, F. Li, H.-M. Cheng, Nanoscale 5 (2013) 1576–1582.
[133] J. Fan, T. Wang, C. Yu, B. Tu, Z. Jiang, D. Zhao, Adv. Mater. 16 (2004) 1432–1436.
[134] Z. Lu, H. Wang, CrystEngComm 16 (2014) 550–555.
[135] A. Mehdinia, E. Ziaei, A. Jabbari, Electrochim. Acta 130 (2014) 512–518.
[136] D. Banerjee, D. Nawn, K. Chattopadhyay, J. Alloys Compd. 572 (2013) 49–55.
[137] X. Liu, M. Wu, M. Li, X. Pan, J. Chen, X. Bao, J. Mater. Chem. A 1 (2013) 9527–9535.
[138] Q.-G. Shao, W.-M. Chen, Z.-H. Wang, L. Qie, L.-X. Yuan, W.-X. Zhang, X.-L. Hu, Y.-H. Huang, Electrochem. Commun. 13 (2011) 1431–1434.
[139] Y. Zhao, J. Li, N. Wang, C. Wu, G. Dong, L. Guan, J. Phys. Chem. C 116 (2012) 18612–18617.
[140] L. Cui, J. Shen, F. Cheng, Z. Tao, J. Chen, J. Power Sources 196 (2011) 2195–2201.
[141] S.-M. Paek, E. Yoo, I. Honma, Nano Lett. 9 (2008) 72–75.
[142] C. Zhong, J. Wang, Z. Chen, H. Liu, J. Phys. Chem. C 115 (2011) 25115–25120.
[143] J. Liang, W. Wei, D. Zhong, Q. Yang, L. Li, L. Guo, ACS Appl. Mater. Interfaces 4 (2012) 454–459.
[144] Y. Li, X. Lv, J. Lu, J. Li, J. Phys. Chem. C 114 (2010) 21770–21774.
[145] S. Prabakar, Y.H. Hwang, E.G. Bae, S. Shim, D. Kim, M.S. Lah, K.S. Sohn, M. Pyo, Adv. Mater. 25 (2013) 3307–3312.
[146] C. Xu, J. Sun, L. Gao, J. Mater. Chem. 22 (2012) 975–979.
[147] X. Huang, X. Zhou, L. Zhou, K. Qian, Y. Wang, Z. Liu, C. Yu, ChemPhysChem 12 (2011) 278–281.
[148] R. Thomas, G. Mohan Rao, Electrochim. Acta 125 (2014) 380–385.
[149] F. Ye, B. Zhao, R. Ran, Z. Shao, Chemistry 20 (2014) 4055–4063.
[150] H. Lu, N. Li, M. Zheng, L. Qiu, S. Zhang, J. Zheng, G. Ji, J. Cao, Mater. Lett. 115 (2014) 125–128.
[151] S. Jiang, B. Zhao, R. Ran, R. Cai, M.O. Tadé, Z. Shao, RSC Adv. 4 (2014) 9367.
[152] Q. Guo, S. Chen, X. Qin, Mater. Lett. 119 (2014) 4–7.
[153] Y. Zhu, C. Li, C. Cao, RSC Adv. 3 (2013) 11860.
[154] A. Dhanabalan, X. Li, R. Agrawal, C. Chen, C. Wang, Nanomaterials 3 (2013) 606–614.
[155] Q. Guo, Z. Zheng, H. Gao, J. Ma, X. Qin, J. Power Sources 240 (2013) 149–154.
[156] Y.-H. Hwang, E.G. Bae, K.-S. Sohn, S. Shim, X. Song, M.S. Lah, M. Pyo, J. Power Sources 240 (2013) 683–690.
[157] Y. Chen, B. Song, R.M. Chen, L. Lu, J. Xue, J. Mater. Chem. A 2 (2014) 5688.
[158] Q. Han, J. Zai, Y. Xiao, B. Li, M. Xu, X. Qian, RSC Adv. 3 (2013) 20573.
[159] Q. Guo, X. Qin, J. Solid State Electrochem. 18 (2013) 1–9.
[160] H. Liu, J. Huang, X. Li, J. Liu, Y. Zhang, K. Du, Appl. Surf. Sci. 258 (2012) 4917–4921.
[161] X. Zhou, Y.-X. Yin, L.-J. Wan, Y.-G. Guo, J. Mater. Chem. 22 (2012) 17456.
[162] S. Yang, W. Yue, J. Zhu, Y. Ren, X. Yang, Adv. Funct. Mater. 23 (2013) 3570–3576.
[163] J. Lin, Z. Peng, C. Xiang, G. Ruan, Z. Yan, D. Natelson, J.M. Tour, ACS Nano 7 (2013) 6001–6006.
[164] J.w. Seo, J.t. Jang, S.w. Park, C. Kim, B. Park, J. Cheon, Adv. Mater. 20 (2008) 4269–4273.
[165] C. Zhai, N. Du, H.Z.D. Yang, Chem. Commun. 47 (2011) 1270–1272.
[166] J. Xia, G. Li, Y. Mao, Y. Li, P. Shen, L. Chen, CrystEngComm 14 (2012) 4279–4283.
[167] Y. Du, Z. Yin, X. Rui, Z. Zeng, X.-J. Wu, J. Liu, Y. Zhu, J. Zhu, X. Huang, Q. Yan, Nanoscale 5 (2013) 1456–1459.
[168] M. He, L.-X. Yuan, Y.-H. Huang, RSC Adv. 3 (2013) 3374–3383.
[169] H. Zhong, G. Yang, H. Song, Q. Liao, H. Cui, P. Shen, C.-X. Wang, J. Phys. Chem. C 116 (2012) 9319–9326.
[170] M.K. Jana, H. Rajendra, A.J. Bhattacharyya, K. Biswas, CrystEngComm 16 (2014) 3994–4000.
[171] Y. Li, J. Tu, X. Huang, H. Wu, Y. Yuan, Electrochim. Acta 52 (2006) 1383–1389.
[172] H. Mukaibo, A. Yoshizawa, T. Momma, T. Osaka, J. Power Sources 119-121 (2003) 60–63.
[173] G. Gnana Kumar, K. Reddy, K.S. Nahm, N. Angulakshmi, A. Manuel Stephan, J. Phys. Chem. Solids 73 (2012) 1187–1190.
[174] Y. Li, J. Tu, X. Huang, H. Wu, Y. Yuan, Electrochem. Commun. 9 (2007) 49–53.
[175] L. Wang, L. Zhuo, Y. Yu, F. Zhao, Electrochim. Acta 112 (2013) 439–447.
[176] T.-J. Kim, C. Kim, D. Son, M. Choi, B. Park, J. Power Sources 167 (2007) 529–535.
[177] M.K. Jana, H.B. Rajendra, A.J. Bhattacharyya, K. Biswas, CrystEngComm 16 (2014) 3994.
[178] A.M. Tripathi, S. Mitra, RSC Adv. 4 (2014) 10358.
[179] J. Li, P. Wu, F. Lou, P. Zhang, Y. Tang, Y. Zhou, T. Lu, Electrochim. Acta 111 (2013) 862–868.
[180] H. Sun, M. Ahmad, J. Luo, Y. Shi, W. Shen, J. Zhu, Mater. Res. Bull. 49 (2014) 319–324.
[181] Q. Wang, Y. Huang, J. Miao, Y. Zhao, W. Zhang, Y. Wang, J. Am. Ceram. Soc. 96 (2013) 2190–2196.
[182] P. Chen, Y. Su, H. Liu, Y. Wang, ACS Appl. Mater. Interfaces 5 (2013) 12073–12082.
[183] K. Chang, Z. Wang, G. Huang, H. Li, W. Chen, J.Y. Lee, J. Power Sources 201 (2012) 259–266.
[184] L. Zhuo, Y. Wu, L. Wang, Y. Yu, X. Zhang, F. Zhao, RSC Adv. 2 (2012) 5084–5087.
[185] J. Yin, H. Cao, Z. Zhou, J. Zhang, M. Qu, J. Mater. Chem. 22 (2012) 23963–23970.
[186] Q. Wang, Y.-X. Nie, B. He, L.-L. Xing, X.-Y. Xue, Solid State Sci. 31 (2014) 81–84.
[187] X. Jiang, X. Yang, Y. Zhu, J. Shen, K. Fan, C. Li, J. Power Sources 237 (2013) 178–186.

[188] N. Du, X. Wu, C. Zhai, H. Zhang, D. Yang, J. Alloys Compd. 580 (2013) 457–464.
[189] L. Ji, H.L. Xin, T.R. Kuykendall, S.L. Wu, H. Zheng, M. Rao, E.J. Cairns, V. Battaglia, Y. Zhang, Phys. Chem. Chem. Phys. (2012).
[190] Q. Zhang, R. Li, M. Zhang, B. Zhang, X. Gou, Electrochim. Acta 115 (2014) 425–433.
[191] M. Sathish, S. Mitani, T. Tomai, I. Honma, J. Phys. Chem. C 116 (2012) 12475–12481.
[192] S. Liu, X. Lu, J. Xie, G. Cao, T. Zhu, X. Zhao, ACS Appl. Mater. Interfaces 5 (2013) 1588–1595.
[193] L. Mei, C. Xu, T. Yang, J. Ma, L. Chen, Q. Li, T. Wang, J. Mater. Chem. A 1 (2013) 8658.
[194] M. Zhang, D. Lei, X. Yu, L. Chen, Q. Li, Y. Wang, T. Wang, G. Cao, J. Mater. Chem. 22 (2012) 23091.
[195] B. Luo, Y. Fang, B. Wang, J. Zhou, H. Song, L. Zhi, Energy Environ. Sci. 5 (2012) 5226.
[196] W. Chen, S. Li, C. Chen, L. Yan, Adv. Mater. 23 (2011) 5679–5683.
[197] B. Qiu, M. Xing, J. Zhang, J. Am. Chem. Soc. 136 (2014) 5852–5855.
[198] L. Liang, Y. Xu, Y. Lei, H. Liu, Nanoscale 6 (2014) 3536–3539.
[199] L. Xiao, D. Wu, S. Han, Y. Huang, S. Li, M. He, F. Zhang, X. Feng, ACS Appl. Mater. Interfaces 5 (2013) 3764–3769.
[200] R. Wang, C. Xu, M. Du, J. Sun, L. Gao, P. Zhang, H. Yao, C. Lin, Small (2014), http://dx.doi.org/10.1002/smll.201303371.
[201] J. Liang, Y. Liu, L. Guo, L. Li, RSC Adv. 3 (2013) 11489.
[202] W. Wang, Y. Xiao, X. Zhao, B. Liu, M. Cao, CrystEngComm 16 (2014) 922–929.
[203] C.T. Cherian, M. Zheng, M.V. Reddy, B. Chowdari, C.H. Sow, ACS Appl. Mater. Interfaces 5 (2013) 6054–6060.
[204] L. Wang, W. Zhang, C. Wang, D. Wang, Z. Liu, Q. Hao, Y. Wang, K. Tang, Y. Qian, J. Mater. Chem. A 2 (2014) 4970–4974.
[205] D. Zhang, S. Zhang, Y. Jin, T. Yi, S. Xie, C. Chen, J. Alloys Compd. 415 (2006) 229–233.
[206] Y. Sharma, N. Sharma, G. Subba Rao, B. Chowdari, Chem. Mater. 20 (2008) 6829–6839.
[207] S. Zhao, Y. Bai, W.-F. Zhang, Electrochim. Acta 55 (2010) 3891–3896.
[208] Y. Chen, B. Qu, L. Mei, D. Lei, L. Chen, Q. Li, T. Wang, J. Mater. Chem. 22 (2012) 25373–25379.
[209] L. Li, S. Peng, J. Wang, Y.L. Cheah, P. Teh, Y. Ko, C. Wong, M. Srinivasan, ACS Appl. Mater. Interfaces 4 (2012) 6005–6012.
[210] L. Li, S. Peng, Y.L. Cheah, J. Wang, P. Teh, Y. Ko, C. Wong, M. Srinivasan, Nanoscale 5 (2013) 134–138.
[211] Q. Wang, Y. Huang, Y. Zhao, W. Zhang, Y. Wang, Surf. Interface Anal. 45 (2013) 1297–1303.
[212] Y. Huang, Q. Wang, Y. Wang, Micro Nano Lett. 7 (2012) 1278–1281.
[213] Q. Wang, Y. Huang, J. Miao, Y. Wang, Y. Zhao, Appl. Surf. Sci. 258 (2012) 6923–6929.
[214] Q. Wang, Y. Huang, J. Miao, Y. Zhao, Y. Wang, Appl. Surf. Sci. 258 (2012) 9896–9901.
[215] Q. Wang, Y. Huang, J. Miao, Y. Zhao, Y. Wang, Mater. Lett. 71 (2012) 66–69.
[216] G. Fang, S. Kaneko, W. Liu, B. Xia, H. Sun, R. Zhang, J. Zheng, D. Li, Appl. Surf. Sci. 283 (2013) 963–967.
[217] Y. Zhao, Y. Huang, Q. Wang, W. Zhang, K. Wang, M. Zong, J. Appl. Electrochem. 43 (2013) 1243–1248.
[218] Y. Zhao, Y. Huang, L. Xue, X. Sun, Q. Wang, W. Zhang, K. Wang, M. Zong, Polym. Test. 32 (2013) 1582–1587.
[219] F. Han, W.C. Li, C. Lei, B. He, K. Oshida, A.H. Lu, Small (2014), http://dx.doi.org/10.1002/smll.201400371.
[220] K. Wang, Y. Huang, T. Han, Y. Zhao, H. Huang, L. Xue, Ceram. Int. 40 (2014) 2359–2364.
[221] S. Yuvaraj, S. Amaresh, Y. Lee, R.K. Selvan, RSC Adv. 4 (2014) 6407–6416.
[222] Y. Zhao, Y. Huang, Q. Wang, K. Wang, M. Zong, L. Wang, X. Sun, Ceram. Int. 40 (2014) 2275–2280.
[223] Y. Cao, L. Zhang, D. Tao, D. Huo, K. Su, Electrochim. Acta 130 (2014) 483–489.
[224] W. Song, J. Xie, W. Hu, S. Liu, G. Cao, T. Zhu, X. Zhao, J. Power Sources 229 (2013) 6–11.
[225] Y. Zhao, Y. Huang, Q. Wang, X. Wang, M. Zong, H. Wu, W. Zhang, Electron. Mater. Lett. 9 (2013) 683–686.
[226] J. Zhang, J. Liang, Y. Zhu, D. Wei, L. Fan, Y. Qian, J. Mater. Chem. A 2 (2014) 2728–2734.
[227] Y. Zhao, Y. Huang, W. Zhang, Q. Wang, K. Wang, M. Zong, X. Sun, RSC Adv. 3 (2013) 23489–23494.
[228] Y. Zhao, Y. Huang, X. Sun, H. Huang, K. Wang, M. Zong, Q. Wang, Electrochim. Acta 120 (2014) 128–132.
[229] R. Liang, H. Cao, D. Qian, J. Zhang, M. Qu, J. Mater. Chem. 21 (2011) 17654–17657.
[230] W. Wang, Q. Hao, W. Lei, X. Xia, X. Wang, RSC Adv. 2 (2012) 10268.
[231] J.-K. Kim, L. Aguilera, F. Croce, J.-H. Ahn, J. Mater. Chem. A 2 (2014) 3551–3556.
[232] J. Wang, L. Lu, D. Shi, R. Tandiono, Z. Wang, K. Konstantinov, H. Liu, ChemPlusChem 78 (2013) 318–324.
[233] F. Han, D. Li, W.C. Li, C. Lei, Q. Sun, A.H. Lu, Adv. Funct. Mater. 23 (2013) 1692–1700.
[234] X. Wang, L. Shen, H. Li, J. Wang, H. Dou, X. Zhang, Electrochim. Acta 129 (2014) 283–289.
[235] X. Liu, H. Li, D. Li, M. Ishida, H. Zhou, J. Power Sources 243 (2013) 374–380.
[236] J. Kim, J.K. Yoo, Y.S. Jung, K. Kang, Adv. Energy Mater. 3 (2013) 1004–1007.
[237] Y. Zhao, Y. Huang, Q. Wang, Ceram. Int. 39 (2013) 6861–6866.
[238] A. Bhaskar, M. Deepa, M. Ramakrishna, T.N. Rao, J. Phys. Chem. C 118 (2014) 7296–7306.
[239] J. Cheng, H. Xin, H. Zheng, B. Wang, J. Power Sources 232 (2013) 152–158.
[240] Z. Li, G. Wu, D. Liu, W. Wu, B. Jiang, J. Zheng, Y. Li, J. Li, M. Wu, J. Mater. Chem. A 2 (2014) 7471–7477.
[241] Y. Su, S. Li, D. Wu, F. Zhang, H. Liang, P. Gao, C. Cheng, X. Feng, ACS Nano 6 (2012) 8349–8356.
[242] C. Zhang, X. Peng, Z. Guo, C. Cai, Z. Chen, D. Wexler, S. Li, H. Liu, Carbon 50 (2012) 1897–1903.
[243] Y. Zhao, Y. Huang, Q. Wang, X. Wang, M. Zong, Ceram. Int. 39 (2013) 1741–1747.
[244] D. Wang, J. Yang, X. Li, D. Geng, R. Li, M. Cai, T.-K. Sham, X. Sun, Energy Environ. Sci. 6 (2013) 2900.
[245] D. Wang, X. Li, J. Yang, J. Wang, D. Geng, R. Li, M. Cai, T.K. Sham, X. Sun, Phys. Chem. Chem. Phys. 15 (2013) 3535–3542.
[246] P. Lian, J. Wang, D. Cai, L. Ding, Q. Jia, H. Wang, Electrochim. Acta 116 (2014) 103–110.
[247] X. Zheng, W. Lv, Y.-B. He, C. Zhang, W. Wei, Y. Tao, B. Li, Q.-H. Yang, J. Nanomater. 2014 (2014) 1–6.
[248] T. Chen, L. Pan, X. Liu, K. Yu, Z. Sun, RSC Adv. 2 (2012) 11719.
[249] Z. Chen, K. Xie, X. Hong, Electrochim. Acta 108 (2013) 674–679.
[250] N. Li, H. Song, H. Cui, G. Yang, C. Wang, J. Mater. Chem. A 2 (2014) 2526.
[251] Y. Zou, X. Zhou, J. Yang, J. Mater. Chem. A 2 (2014) 4524.
[252] J. Zhu, D. Lei, G. Zhang, Q. Li, B. Lu, T. Wang, Nanoscale 5 (2013) 5499–5505.
[253] Y. Zou, X. Zhou, J. Xie, Q. Liao, B. Huang, J. Yang, J. Mater. Chem. A 2 (2014) 4524.
[254] H. Yang, T. Song, S. Lee, H. Han, F. Xia, A. Devadoss, W. Sigmund, U. Paik, Electrochim. Acta 91 (2013) 275–281.
[255] G. Xia, N. Li, D. Li, R. Liu, C. Wang, Q. Li, X. Lü, J.S. Spendelow, J. Zhang, G. Wu, ACS Appl. Mater. Interfaces 5 (2013) 8607–8614.
[256] W. Xing, X. Wang, L. Song, S. Li, C. Chen, Y. Hu, Mater. Chem. Phys. 140 (2013) 441–446.
[257] J. Zhu, D. Wang, L. Wang, X. Lang, W. You, Electrochim. Acta 91 (2013) 323–329.
[258] Z. Chen, M. Zhou, Y. Cao, X. Ai, H. Yang, J. Liu, Adv. Energy Mater. 2 (2012) 95–102.
[259] S. Liu, R. Wang, M. Liu, J. Luo, X. Jin, J. Sun, L. Gao, J. Mater. Chem. A 2 (2014) 4598.
[260] X. Jiang, X. Yang, Y. Zhu, K. Fan, P. Zhao, C. Li, New J. Chem. 37 (2013) 3671.
[261] B.P. Vinayan, S. Ramaprabhu, J. Mater. Chem. A 1 (2013) 3865.
[262] X. Wang, Q. Weng, X. Liu, X. Wang, D.M. Tang, W. Tian, C. Zhang, W. Yi, D. Liu, Y. Bando, D. Golberg, Nano Lett. 14 (2014) 1164–1171.
[263] C. Xu, J. Sun, L. Gao, Nanoscale 4 (2012) 5425–5430.
[264] X. Zhou, J. Bao, Z. Dai, Y.-G. Guo, J. Phys. Chem. C 117 (2013) 25367–25373.
[265] Z. Zhu, S. Wang, J. Du, Q. Jin, T. Zhang, F. Cheng, J. Chen, Nano Lett. 14 (2014) 153–157.
[266] X. Wang, X. Cao, L. Bourgeois, H. Guan, S. Chen, Y. Zhong, D.-M. Tang, H. Li, T. Zhai, L. Li, Y. Bando, D. Golberg, Adv. Funct. Mater. 22 (2012) 2682–2690.
[267] X. Zhou, L.J. Wan, Y.G. Guo, Adv. Mater. 25 (2013) 2152–2157.
[268] R. Wang, C. Xu, J. Sun, L. Gao, H. Yao, ACS Appl. Mater. Interfaces 6 (2014) 3427–3436.
[269] F. Xiao, J. Song, H. Gao, X. Zan, R. Xu, H. Duan, ACS Nano 6 (2011) 100–110.
[270] N. Mahmood, C. Zhang, F. Liu, J. Zhu, Y. Hou, ACS Nano 7 (2013) 10307–10318.